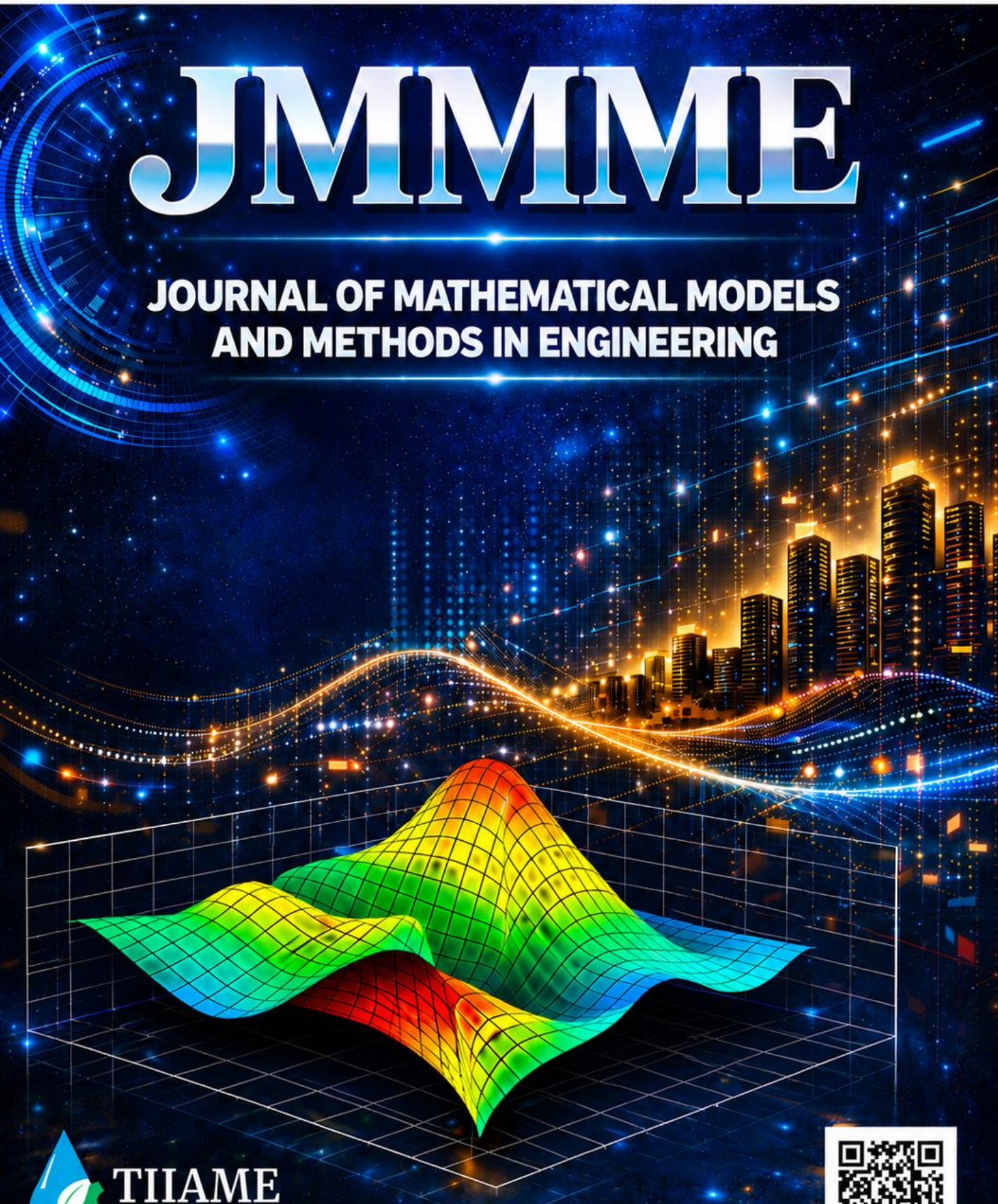
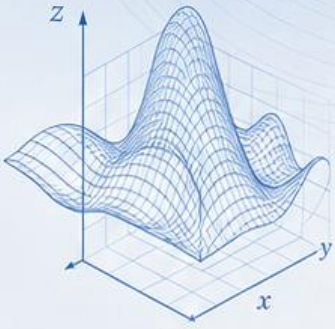
INTERNATIONAL STANDARD SERIAL NUMBER INTERNATIONAL CENTRE
Google Scholar
zenodo
doi
OpenAIRE
OPEN ACCESS

JMMME

JOURNAL OF MATHEMATICAL MODELS AND METHODS IN ENGINEERING



TIIAME
National Research University



JMMME

JOURNAL OF MATHEMATICAL MODELS AND METHODS IN ENGINEERING

$$\frac{dx}{dt} = Ax + b(t)$$

$$\frac{\partial u}{\partial t} = \alpha \nabla^2 u + f$$

$$\sum_{i=1}^{n} a_i x_i + b$$

$$f(x) = \int_a^b f(x)\,dx$$

$$A = \begin{bmatrix} a_{11} & a_{12} & \cdots & a_{1n} \\ a_{21} & a_{22} & \cdots & a_{2n} \\ \vdots & \vdots & \ddots & \vdots \\ a_{n1} & a_{n2} & \cdots & a_{nn} \end{bmatrix}$$

JOURNAL INFORMATION

"Journal of Mathematical Models and Methods in Engineering" is an international, peer-reviewed, and open-access scientific journal established in the Republic of Uzbekistan by the National Research University "Tashkent Institute of Irrigation and Agricultural Mechanization Engineers" under Certificate No. 1648073 dated June 15, 2026.

$$\sum_{i=1}^{n} w_i x_i$$

The journal specializes in publishing scientific research on mathematical modeling, numerical methods, computational algorithms, optimization, and analytical approaches across various fields of engineering — including civil engineering, mechanical engineering, energy, hydraulic engineering, materials science, robotics, and environmental protection. It serves as a scientific platform for scholars, engineers, educators, and doctoral researchers to exchange theoretical and applied knowledge.



All submitted manuscripts undergo a double-blind peer review process and are published in strict compliance with high academic quality standards and publication ethics.



The journal has been published since June 15, 2026, once per quarter, that is, 4 times per year. Manuscripts are accepted in English and must be prepared in accordance with international IMRAD standards.

TIIAME
National Research University

FOUNDER	TIIAME National Research University
ADDRESS	39 Qori-Niyoziy Street, Mirzo Ulugbek District, Tashkent, Republic of Uzbekistan
PHONE	+998 (93) 397-12-39
WEBSITE	jmmme.uz
CERTIFICATE	No. 1648073, June 15, 2026
PUBLISHED	2026-06-15
LANGUAGE	English
FREQUENCY	Quarterly / 4 times per year
REVIEW	Double-blind peer review
STANDARD	International IMRAD standards

0 1 0 1
1 0 1 0
0 1 0 1
1 0 1 1
1 1 0 1
1 1 0 1
0 1 1 0
0 0 1 1
1 1 0 1
1 1 1 1
2 0 2 2
1 2 1 1

INDEXED AND DISCOVERABLE THROUGH

ISSN INTERNATIONAL STANDARD SERIAL NUMBER | Google Scholar | zenodo | doi | OpenAIRE | OPEN ACCESS

JMMME

TIIAME National Research University

JOURNAL OF MATHEMATICAL MODELS AND METHODS IN ENGINEERING

EDITOR-IN-CHIEF

Xudayarov Baxtiyar Alimovich

Doctor of Technical Sciences, Professor

TIIAME National Research University, Tashkent, Republic of Uzbekistan

ASSOCIATE EDITOR

Abdullayev Akmaljon Abdujalilovich

PhD, Associate Professor, Department of Higher Mathematics

TIIAME National Research University, Tashkent, Republic of Uzbekistan

COMPUTER OPERATOR AND DESIGNER

Sattarov Ulug'bek Umed o'g'li

EDITORIAL BOARD MEMBERS

Turayev Fozil Jurakulovich
Head of the Department of Higher Mathematics, Associate Professor
TIIAME National Research University, Tashkent, Republic of Uzbekistan

Ergashev Tukhtasin Gulomjonovich
Doctor of Physical and Mathematical Sciences, Professor
TIIAME National Research University, Tashkent, Republic of Uzbekistan

Eshkuvatov Zaynidin Karimovich
Doctor of Physical and Mathematical Sciences, Professor
TIIAME National Research University, Tashkent, Republic of Uzbekistan

Eshmatov Baxtiyor Xasanovich
Doctor of Physical and Mathematical Sciences, Associate Professor
TIIAME National Research University, Tashkent, Republic of Uzbekistan

INTERNATIONAL SUBJECT EDITORS

Andriy Verlan
Associate Professor, Department of Manufacturing and Civil Engineering, Norwegian University of Science and Technology (NTNU), Trondheim, Norway.

Dr. Mohd Kamal Mohd Nawawi
PhD, Associate Professor, School of Quantitative Sciences, Universiti Utara Malaysia, Kedah, Malaysia.

Vatin Nikolay Ivanovich
Doctor of Technical Sciences, Professor, Peter the Great St. Petersburg Polytechnic University.

Norihan Md Arifin
Professor of Applied Mathematics, Head of the Department of Mathematics and Statistics, Universiti Putra Malaysia, Selangor, Malaysia.

Sergey Leonov
Doctor of Engineering, Professor at National Technical University "Kharkiv Polytechnic Institute".

Amarjit Singh
PhD, Department of Mechanical Engineering, National Institute of Technology Hamirpur HP, India.

Vishesh Ranjan Kar
Assistant Professor, Department of Mechanical Engineering, National Institute of Technology Jamshedpur, India.

Muhammad Suzuri Hitam
Professor, Faculty of Computer Science and Mathematics, University Malaysia Terengganu, Malaysia.

Tkachenko Oleg Pavlovich
Doctor of Physical and Mathematical Sciences, Associate Professor, Leading Researcher at the Computing Center of the Far Eastern Branch of the Russian Academy of Sciences, Khabarovsk, Russia.

Gobithaasan Rudrusamy
Assoc. Prof. Dr. of School of Mathematical Sciences, University Sains Malaysia, Penang, Malaysia.

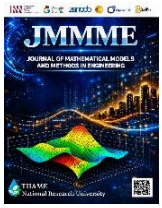
Prof. Dr. Muhammad Zaini Bin Ahmad
Doctor of Industrial Computing, Professor, Department of Mathematical Sciences, Faculty of Intelligent Computing, Universiti Malaysia Perlis, Malaysia.

Mahmoud Mohamed Selim Saleh
Doctor of Applied Mathematics, Professor, College of Science and Humanities, Prince Sattam bin Abdulaziz University, Al-Kharj, Saudi Arabia.

Pradeep G. Siddheshwar
M.Sc., Ph.D. Senior Professor of Mathematics, Bangalore 560 029, India.

Journal of Mathematical Models and Methods in Engineering

journal homepage:
https://jmmme.uz/index.php/journal



Optimization of Heat Transfer in MHD Mixed Convection Hybrid Nanofluid Flow Over a Shrinking Plate Using Response Surface Methodology.

Nor Ain Azeany Mohd Nasir[1,2], Nur Fatin Irwani Muhammad Fadzil[3], Norihan Md Arifin[2,3,*], Rusya Iryanti Yahaya[2], Nur Syahirah Wahid[3], and Mohd Syazwan Mohamad Anuar[1]

[1]Department of Mathematics, Centre for Defence Foundation Studies, Universiti Pertahanan Nasional Malaysia, Kem Sungai Besi 57000 Kuala Lumpur, Malaysia.
[2]Institute for Mathematical Research, Universiti Putra Malaysia, 43400 UPM Serdang, Selangor, Malaysia.
[3]Department of Mathematics and Statistics, Faculty of Science, Universiti Putra Malaysia, 43400 UPM, Serdang, Selangor

ARTICLE INFO

Article history:
Received 15 October 2026
Received in revised form 21 October 2026
Accepted 28 October 2026
Available online 1 November 2026

Keywords:

Hybrid nanofluid; mixed convection; nanoparticle shape; Response Surface Methodology

ABSTRACT

This study focuses on optimizing the heat transfer performance of magnetohydrodynamic (MHD) mixed convection flow of a hybrid nanofluid (MgO–Ag/H_2O) over a shrinking plate, with a focus on nanoparticle shape effects. The governing equations, which are based on boundary layer theory, are reduced to a system of nonlinear ordinary differential equations through similarity transformations and are computed numerically for this purpose. The governing partial differential equations are first reduced to ordinary differential equations using similarity transformations. The resulting ODEs are then solved numerically using the bvp4c built-in solver in MATLAB software. The findings of this study reveal significant insights into the influence of nanoparticle shapes, MgO concentration, and magnetic parameters on various flow and heat transfer characteristics. It is observed that cylindrical nanoparticles exhibit higher skin friction and Nusselt numbers compared to brick and spherical nanoparticles. Moreover, an increase in MgO concentration leads to higher skin friction but lower Nusselt numbers. For opposing flow, a decrease in the magnetic parameter correlates with reduced skin friction and Nusselt numbers, while an increase in the magnetic parameter during assisting flow results in higher skin friction and Nusselt numbers. Additionally, spherical-shaped nanoparticles demonstrate the highest velocity and temperature profiles, whereas an increase in MgO concentration causes a reduction in velocity and temperature profiles. Using Response Surface Methodology (RSM), the optimized combination of Ag and MgO concentrations and magnetic parameters is determined to achieve the highest skin friction and Nusselt numbers. The desirability of 99.95% and 99.98% is achieved for skin friction and Nusselt numbers, respectively, highlighting the effectiveness of the proposed approach in optimizing flow and heat transfer characteristics under different flow conditions.

1. Introduction

Mixed-convection hybrid nanofluids have gained significant attention in recent years due to their potential to enhance heat transfer performance across various engineering applications. These

*Corresponding author: Institute for Mathematical Research, Universiti Putra Malaysia, 43400 UPM Serdang, Selangor, Malaysia

nanofluids combine traditional fluids and nanoparticles, offering unique thermal properties that can be tailored to specific needs. The study of mixed-convection hybrid nanofluids builds upon extensive research on conventional nanofluids and mixed-convection flows. Based on Mahmood *et al*. [1], the mixed convection parameter within the flow domain, alongside factors such as mass suction, magnetic parameter, and velocity slip parameter, can influence the skin friction and heat transfer properties of the hybrid nanofluid. This finding is also reported by Jamrus *et al*. [2]. They claimed that the Nusselt number showed a slight rise of about 0.21% with an increase in the magnetic parameter during mixed convection flow. Moreover, Ummeda and Ontela [3] claimed that nanoparticle distribution and interactions with the fluid affect the entropy generation at the left and right surfaces. On the left surface, increased nanoparticle volume boosts interactions and friction in the boundary layer, heightening entropy generation due to nanoparticle effects on momentum and heat transfer mechanisms near the surface. Conversely, the dominant fluid flow mechanism near the right surface diminishes nanoparticle influence, leading to reduced entropy generation. However, Paul *et al*. [4] reported that the Richardson parameter significantly enhances local skin friction and improves thermal and mass transfer rates. According to Yadav *et al*. [5], an increase in the magnetic control parameter within the hybrid nanofluid regime in opposing flow conditions leads to improvements in the thermal boundary layer thickness while decreasing convective heat transfer. Numerous researchers have investigated mixed convection hybrid nanofluid flows in various scenarios, resulting in diverse findings. For instance, Rajarathinam et al. [6] and Abood *et al.* [7] studied flow over inclined porous cavities, Zhang *et al*. [8] explored flow with Stefan's blowing effect, Hameed *et al*. [9] analysed flow inside an oval-shaped annulus, and Mustafa *et al*. [10] investigated flow in a rectangular cavity. The application of mixed convection hybrid nanofluids spans various engineering fields, including thermal management in electronic devices, heat exchangers, solar energy systems, and aerospace applications. Understanding the behaviour of mixed convection hybrid nanofluids is crucial for addressing challenges related to thermal management, energy efficiency, and sustainability. Researchers can develop innovative solutions to enhance heat transfer processes and address emerging technological needs by exploring the interaction between nanoparticles and fluid flow in mixed convection environments.

The application of magnetic fields in enhancing fluid flow and heat transfer processes has garnered significant interest in recent years, particularly in the context of hybrid nanofluids. Hybrid nanofluids, which combine nanoparticles with conventional fluids, offer unique opportunities for optimising heat transfer rates and improving thermal management in various engineering applications. Hussain *et al*. [11] mentioned that in their research, maintaining the magnetization inclination angle at 60 degrees and the magnetic force within the range of 0.5 to 4 increased the velocity profile. A similar finding is reported by Dinarvand *et al*. [12], who claimed that the application of a magnetic field in a horizontal direction exhibits the highest temperature distribution and heat transfer rate. This finding, also supported by Sundar and Ramana [13], explained that with a nanofluid volume fraction of 1.0% and a magnetic field strength of 4000 G, the Nusselt number increases by 41.03% compared to the nanofluid without any magnetic field. Giwa *et al*. [14] found that applying a magnetic stimulus led to an improved thermal transport performance in hybrid nanofluids based on the brine. Many researchers have investigated the impact of magnetic fields on hybrid nanofluids flow and heat transfer, including studies by Mahabaleshwar *et al*. [15], Sundar *et al*. [16], Rajesh and Oztop [17], and Khan *et al*. [18]. The application of magnetic field effects on hybrid nanofluid flow and heat transfer is relevant to various engineering disciplines, including thermal management in electronics, energy systems, and heat exchangers. By leveraging the magnetic properties of nanoparticles and the influence of magnetic fields, researchers and engineers can design efficient heat transfer systems with improved performance and energy savings. Understanding the behaviour of hybrid nanofluids under magnetic fields is crucial for optimizing heat transfer processes, improving energy efficiency, and addressing challenges related to thermal management.

Fluid flow and heat transfer over shrinking surfaces are fundamental phenomena encountered in various engineering applications, including cooling systems, thermal management, and heat

exchangers. Understanding the behaviour of fluids in such configurations is crucial for optimising heat transfer rates, improving energy efficiency, and designing efficient thermal control systems. According to Dero *et al*. [19], there is a rising trend in the effects of nanoparticle solid volume fraction and shrinking parameters on velocity and thermal fields. On the other hand, Yahaya et al. [20] found that increasing the shrinking parameter results in higher velocity and temperature profiles, while reducing the secondary and ternary velocity profiles in the case of a biaxial stretching/shrinking permeable surface. Hafeez *et al*. [21] concurred with Dero et al., adding that the temperature of the liquid rises with an increase in the Biot number and thermal radiation. Jaafar et al. [22] investigated the heat transfer enhancement of a hybrid nanofluid on an exponentially stretching/shrinking surface. They observed that the Cu–TiO2/water hybrid nanofluid improved heat transfer by 4.04% compared to water, while the Cu/water nanofluid showed a heat transfer enhancement of 2.13%. Furthermore, Yasir et al. [23] stated that shear stress decreases by as much as 8.67% in the first solution branch due to the more significant impact of the magnetic parameter, but it increases by approximately 15.61% in the second solution branch. Several additional studies have investigated fluid flow and heat transfer over shrinking surfaces, each exploring different effects and characteristics. These include the study of non-linearly shrinking sheets by Waini *et al*. [24], shrinking cylinder surfaces by Roy and Akter [25], shrinking sheets with colloidal combinations with base fluid features by Saleem *et al*. [26], and the investigation of power law stretching/shrinking sheets by Shah *et al*. [27]. The application of fluid flow and heat transfer over shrinking surfaces is relevant to a wide range of engineering applications, including the cooling of electronic devices, heat exchangers in power plants, aerospace systems, and biomedical devices. By studying the behaviour of fluids in shrinking environments, researchers and engineers can develop innovative solutions for thermal management, energy efficiency, and heat dissipation. Understanding the complexities of fluid flow and heat transfer over shrinking surfaces is critical for optimising heat transfer rates, reducing energy consumption, and improving system performance.

The shape of nanoparticles plays a crucial role in influencing the flow and heat transfer characteristics of hybrid nanofluids, which are composite fluids containing nanoparticles dispersed in conventional fluids. Understanding how nanoparticle shape affects flow patterns, heat transfer rates, and thermal performance is essential for optimising hybrid nanofluid engineering systems. The study of nanoparticle shape effects on hybrid nanofluid flow and heat transfer builds upon extensive research in nanofluids, fluid dynamics, and heat transfer enhancement techniques. Different nanoparticle shapes, such as spherical, cylindrical, and brick-shaped, exhibit distinct flow behaviours and interactions with the surrounding fluid. These variations in shape can significantly influence flow patterns, turbulence, and heat transfer coefficients in hybrid nanofluids. Asifa *et al*. [28] stated that the use of lamina-shaped nanoparticles could maximise the thermal efficiency of kerosene oil. Anwar *et al*. [29] examined five distinct nanoparticle shapes and determined that blade-shaped hybrid nanoparticles are the most effective in considerably enhancing the heat transfer rate. Rafique et al. [30] investigated five nanoparticle shapes, including oblate spheroids (Os), platelets, blades, cylinders, and bricks made of alumina. They observed that the oblate spheroid (Os)-shaped nanoparticle nanofluid exhibited a higher increase in thermal entropy on the cold fluid side. In contrast, Kezzar *et al*. [31] examined four nanoparticle shapes, including spheres, bricks, cylinders, and platelets. Their findings indicated that hybrid nanofluids containing platelet-shaped nanoparticles had the lowest skin friction coefficient. Recent studies on the impact of nanoparticle shapes were examined by Rahman *et al*. [32], Jeevankumar and Sandeep [33], Ragupathi et al. [34], and Yahyaee [35]. The application of nanoparticle shape effects on hybrid nanofluid flow and heat transfer has broad implications across various engineering disciplines. By understanding and manipulating nanoparticle shapes, researchers and engineers can tailor hybrid nanofluids' thermal properties and heat transfer performance for specific applications. This includes enhancing heat exchangers, improving cooling systems, and optimizing thermal management in electronic devices, aerospace systems, and renewable energy technologies. Understanding the behaviour of hybrid nanofluids with different nanoparticle shapes is

crucial for optimizing heat transfer processes, improving energy efficiency, and addressing challenges related to thermal management.

Based on the above-mentioned literature, this study aims to examine the hybrid nanofluid flow and heat transfer of magnetohydrodynamic (MHD) at the stagnation point on a shrinking sheet. The impacts involved in this study are assumed to be mixed convection flow, Joule heating, and nanoparticle shape factor. The governing equations derived based on the problem mentioned above are then reduced to higher-order ordinary differential equations (ODEs) coupled with a boundary value problem. The ODEs are then solved using the famous solver called bvp4c, which is built into MATLAB software. The stability of the solutions has been shown by Wahid *et al*. [36]. Hence, the results for the second solution will not be discussed but will still be reported since the flow might be useful in the future and to avoid the misinterpretation of the flow and heat transfer characteristics [37].

2. Mathematical Modeling

The MHD stagnation-point flow of hybrid nanofluid resulting from a shrinking sheet with nanoparticle shape impact is depicted in Figure 1. The x and y axes are in Cartesian coordinates, with the x-axis measured along the sheet and the y-axis normal to it. The flow started at $y \geq 0$. It is assumed that the inviscid flow has a velocity of $u_e(x)$, whereas the shrinking sheet has a velocity of $u_w(x)$. Assuming that the temperature of the melting sheet is T_m, the free-stream temperature is T_∞, and the transverse magnetic field's surface-normal direction is B_0.

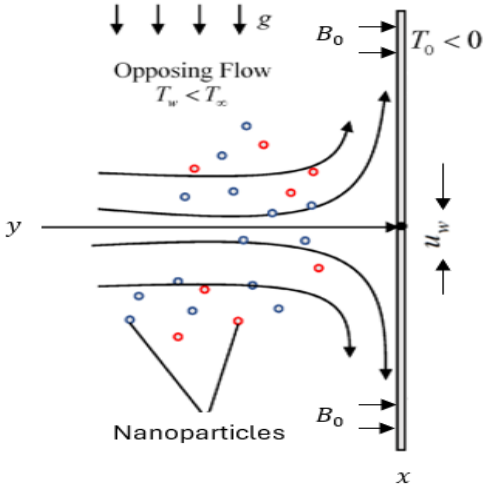


Fig 1. Physical model fo.r a shrinking plate with a magnetic field acting on the surface.

The appropriate governing equations that regulate the flow assumptions are: the mass conservation, the momentum, and the energy equations, which can be derived as (refer to Wahid et al. (2023))

$$\frac{\partial u}{\partial x} + \frac{\partial v}{\partial y} = 0, \tag{1}$$

$$u\frac{\partial u}{\partial x} + v\frac{\partial u}{\partial y} = u_e\frac{du_e}{dx} + \frac{\mu_{hnf}}{\rho_{hnf}}\left(\frac{\partial^2 u}{\partial y^2}\right) - \frac{\sigma_{hnf}{B_0}^2}{\rho_{hnf}}(u - u_e) + \frac{g(\rho\beta)_{hnf}}{\rho_{hnf}}(T - T_\infty), \tag{2}$$

$$u\frac{\partial T}{\partial x} + v\frac{\partial T}{\partial y} = \frac{k_{hnf}}{(\rho C_p)_{hnf}}\left(\frac{\partial^2 T}{\partial y^2}\right) + \frac{\mu_{hnf}}{(\rho C_p)_{hnf}}\left(\frac{\partial u}{\partial y}\right)^2 + \frac{\sigma_{hnf}{B_0}^2}{(\rho C_p)_{hnf}}(u - u_e)^2. \tag{3}$$

The boundary conditions for the above problem are given as follows:

$$u = u_w(x) = cx, \quad v = 0, \quad T = T_m \quad \text{at } y = 0$$
$$u \to u_e(x) = ax, \quad T \to T_\infty \quad \text{as } y \to \infty \tag{4}$$

It should be noted that $\mu, \rho, \sigma, \rho C_p, k$ and $\rho\beta$ stand for dynamic viscosity, density, electrical conductivity, heat capacity, thermal conductivity, and thermal expansion coefficient, respectively. The subscript hnf refers to hybrid nanofluid, where ϕ_1 and $\phi_2$are the nano-particles volume percentages for magnesium oxide (MgO) and silver (Ag). The base fluid is chosen to be H_2O (water). Since this research aims to analyse the impact of nanoparticle shape m. Table 1 shows the relationship between hybrid nanofluid thermophysical properties and nanoparticle shape factors. The values for calculating the hybrid nanofluid thermophysical properties in Table 1 are given in Table 2. It is also vital to acquire the values for the shape factor m for various nanoparticle shapes. Table 3 shows the appropriate values m according to nanoparticle shapes.

Table 1

Relationship between hybrid nanofluid thermophysical properties and nanoparticles shape factors. (Ref. Sarfraz et al. (2023))

Properties	**Hybrid nanofluid with shape factor**
Density	$\frac{\rho_{hnf}}{\rho_f} = (1-\varphi_2)\left[(1-\varphi_1) + \varphi_1\frac{\rho_{s1}}{\rho_f}\right] + \varphi_2\frac{\rho_{s2}}{\rho_f}$
Dynamic viscosity	$\frac{\mu_{hnf}}{\mu_f} = 1 + A_1\varphi_{hnf} + A_2{\varphi_{hnf}}^2$ where $\varphi_{hnf} = \varphi_1 + \varphi_2$
Electrical Conductivity	$\frac{\sigma_{hnf}}{\sigma_{nf}} = \frac{\sigma_{s2}+2\sigma_{nf}-2\varphi_2(\sigma_{nf}-\sigma_{s2})}{\sigma_{s2}+2\sigma_{nf}+\varphi_2(\sigma_{nf}-\sigma_{s2})}$ where $\frac{\sigma_{nf}}{\sigma_f} = \frac{\sigma_{s1}+2\sigma_f-2\varphi_1(\sigma_f-\sigma_{s1})}{\sigma_{s1}+2\sigma_f+\varphi_1(\sigma_f-\sigma_{s1})}$
Heat capacity	$\frac{(\rho C_p)_{hnf}}{(\rho C_p)_f} = (1-\varphi_2)\left[(1-\phi_1) + \varphi_1\frac{(\rho C_p)_{s1}}{(\rho C_p)_f}\right] + \varphi_2\frac{(\rho C_p)_{s2}}{(\rho C_p)_f}$
Thermal conductivity	$\frac{k_{hnf}}{k_{nf}} = \frac{k_{s2}+(m-1)k_{nf}-(m-1)(k_{nf}-k_{s2})\varphi_2}{k_{s2}+(m-1)k_{nf}+(k_{nf}-k_{s2})\varphi_2}$ where $\frac{k_{nf}}{k_f} = \frac{k_{s1}+(m-1)k_f-(m-1)(k_f-k_{s1})\varphi_1}{k_{s1}+(m-1)k_f+(k_f-k_{s1})\varphi_1}$
thermal expansion coefficient	$\frac{(\rho\beta)_{hnf}}{(\rho\beta)_f} = (1-\varphi_2)\left[(1-\varphi_1) + \frac{(\rho\beta)_{s1}}{(\rho\beta)_f}\phi_1\right] + \frac{(\rho\beta)_{s2}}{(\rho\beta)_f}\varphi_2$

Table 2.

Values for calculating the thermophysical properties of MgO, Ag, and H_2O. (Ref. Redouane et al. (2022))

Thermophysical Properties	**MgO**	**Ag**	**H_2O**
Dynamic viscosity μ $(kgm^{-1}s^{-1})$	-	-	0.000855
Density ρ (kgm^{-2})	3560	10500	997.1
Electrical Conductivity σ (Sm^{-1})	5.392×10^{-7}	6.3×10^{7}	0.05

Specific Heat capacity $C_p\ (Jkg^{-1}K^{-1})$	955	235	4179
Thermal conductivity $k\ (Wm^{-1}K^{-1})$	45	429	0.613
Thermal expansion coefficient $\beta(K^{-1})$	3.36×10^{-5}	5.4×10^{-5}	21.0×10^{-5}

Table 3
Values of the shape factor m for several nanoparticle shapes. (Ref. Alabdulhadi et al. (2023))

Nanoparticle shape	**Shape factor** (m)	**Parameters** $(A_1$ & $A_2)$	**Shape**
Brick	3.7	$A_1 = 1.9, A_2 = 471.4$	
Cylindrical	4.9	$A_1 = 13.5, A_2 = 904.4$	
Spherical	3.0	$A_1 = 2.5, A_2 = 6.5$	

By reducing Eqs. (1)–(4) to ordinary differential equations via the similarity transformation, one can obtain solutions for them. Introducing the set of dimensionless variables used in this work (see Wahid et al. (2023)

$$\psi = \sqrt{av_f}xf(\eta), \quad \theta(\eta) = \frac{T - T_m}{T_m - T_\infty}, \quad \eta = \sqrt{\frac{a}{v_f}}y \tag{5}$$

The velocity components which can be associated with the stream function are given as

$$u = axf'(\eta), \quad v = -\sqrt{av_f}f(\eta) \tag{6}$$

Differentiating and substituting equations (5) and (6) into equations (1) – (4) will produce new equations,

$$\frac{\mu_{hnf}/\mu_f}{\rho_{hnf}/\rho_f}f''' + f\,f'' + 1 - f'^2 - \frac{\frac{\sigma_{hnf}}{\sigma_f}}{\frac{\rho_{hnf}}{\rho_f}}M(f' - 1) + \alpha\frac{(\rho\beta)_{hnf}}{(\rho\beta)_f}\theta = 0, \tag{7}$$

$$\frac{1}{(\rho C_p)_{hnf}/(\rho C_p)_f}\left(\frac{k_{hnf}/k_f}{Pr}\theta'' + Ec\left[\frac{\mu_{hnf}}{\mu_f}f''^2 + \frac{\sigma_{hnf}}{\sigma_f}M\,(f' - 1)^2\right]\right) + f\,\theta' = 0, \tag{8}$$

subject to boundary conditions,

$$f(0) = 0, \quad f'(0) = \lambda, \quad \theta(0) = 0 \quad \text{at} \quad \eta = 0,$$
$$f'(\eta) \to 1, \quad \theta(\eta) \to 1 \quad \text{as} \quad \eta \to \infty. \tag{9}$$

The parameters associated with equations (7)–(9) are the magnetic parameter $\left(M = \frac{\sigma_f {B_o}^2}{\rho_f a}\right)$, and mixed convection parameter $\left(\alpha = \frac{Gr_x}{Re_x}\right)$ which $\alpha > 0$ is assumed as assisting flow and $\alpha < 0$ is noted as opposing flow, Prandtl number $\left(Pr = \frac{(\mu C_p)_f}{k_f}\right)$, Eckert number $\left(Ec = \frac{{u_e}^2}{(C_p)_f (T_m - T_\infty)}\right)$, and shrinking/stretching parameter (λ) which $\lambda > 0$ is known as stretching surface and $\lambda < 0$ noted as shrinking surface. Thus, the critical physical quantities involved in this model are given as follows: Skin friction

$$C_f = \frac{\mu_{hnf}}{\rho_f {u_e}^2} \left(\frac{\partial u}{\partial y}\right)_{y=0}, \tag{10}$$

and local Nusselt number $Nu_x = -\frac{x k_{hnf}}{k_f (T_w - T_\infty)} \left(\frac{\partial T}{\partial y}\right)_{y=0}$.

Arranging equation (10) and substituting equation (5) gives,

$${Re^{1/2}}_x \, C_f = \frac{\mu_{hnf}}{\mu_f} f''(0) \quad \text{and} \quad {Re_x}^{-1/2} \, Nu_x = -\frac{k_{hnf}}{k_f} \theta'(0) \tag{11}$$

where $Re_x = u/v_f$ is Reynold's number.

3. Results and Discussions.

The mathematical model that builds up from Eqs. (7) and (8) is actively solved using the bvp4c solver in MATLAB software while adhering to the specified boundary conditions (9). This numerical solver is widely used in mathematics and engineering to solve boundary value problems (BVPs) associated with ordinary differential equations. This solver uses a finite difference method that utilises the three-stage Lobatto IIIa formula with 4th-order accuracy. In this study, solutions are sought at both the upper and lower limits by establishing a boundary layer thickness denoted as η∞ at 15, which is sufficient to satisfy the far-field boundary conditions asymptotically. Meanwhile, a tolerance threshold 10^{-10} is implemented to regulate the solver's precision and determine when it converges to a satisfactory solution. The current problem may have dual solutions; therefore, the bvp4c solver requires initial guesses. These initial guesses are chosen through a trial-and-error process and are iteratively refined if solver convergence is not achieved. Finding the first solution is straightforward, even when bvp4c is provided with a weak initial guess. However, obtaining a suitable initial guess for the second solution poses a challenge. Leveraging the bvp4c solver in MATLAB software, the individual equations, such as the momentum equation (7) and energy equation (8), together with the boundary conditions (9), are numerically solved. Both tables and figures will display the numerical results. Table 4 shows the relative values of the reduced skin friction coefficient for various values of α when$\phi_1 = \phi_2 = M = Ec = 0$. These results suggest a strong correlation between the current findings and those from earlier research by Wahid *et al*. [1] and Bachok *et al*. [5]. The current problem can be solved with confidence using the existing numerical approach. It is worth mentioning that the parameters for nanoparticle

concentration taken for this research are $0.0 \leq \varphi_1, \varphi_2 \leq 0.04$, the magnetic parameter $0.0 \leq M \leq 0.1$, the shrinking parameter $-1.34 \leq \lambda \leq -1.2$ as well as the Eckert number $Ec = 0.01$.

Table 4.
Numerical solution for skin friction when $\varphi_1 = \varphi_2 = M = Ec = \alpha = 0$ and $Pr = 6.2$ (water).

λ	Wahid *et al*. [36]		Bachok *et al*. [41]		Current solution	
	Upper solution	Lower solution	Upper solution	Lower solution	Upper solution	Lower solution
-0.25	1.402240767	-	1.4022408	-	1.402785769	-
-0.5	1.49566972	-	1.4956698	-	1.496180025	-
-0.75	1.489298191	-	1.4892983	-	1.489732265	-
-1.0	1.328816836	0.0	1.328817	0.0	1.329106561	0.0
-1.1	1.186680244	0.049228947	1.1866805	0.049229	1.186898793	0.049228945
-1.15	1.082231123	0.116702139	1.0822315	0.1167022	1.082415493	0.116701975
-1.2	0.932473307	0.233649729	0.9324739	0.2336497	0.932628011	0.233647452
-1.2465	0.584281454	0.554296147	0.5842956	0.5542825	0.585131105	0.553572283
-1.24657	0.574525263	0.564003924	0.5639733		0.576528668	0.562134962

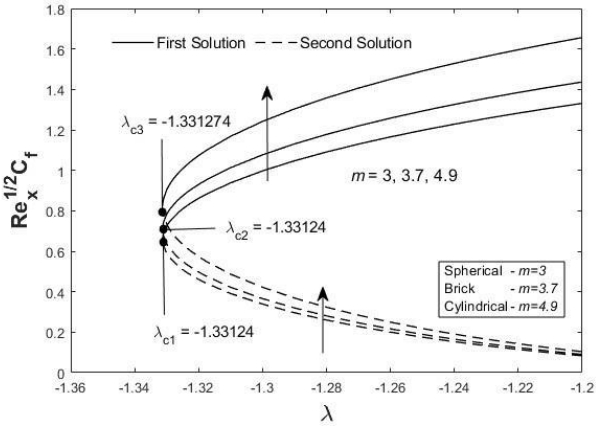


Fig. 2. Skin friction variation with different types of nanoparticle shapes for the shrinking surface.

Figure 2 demonstrates the correlation between nanoparticle morphologies and skin friction. It indicates that spherical nanoparticles have the lowest skin friction, whereas cylindrical nanoparticles have the highest skin friction. This discovery may be elucidated by examining the fluid dynamics and the interaction between the nanoparticles and the surrounding fluid flow. The spherical nanoparticles with reduced skin friction are due to their smooth, rounded surface, which reduces surface roughness and imperfections. When fluid passes over spherical nanoparticles, the streamlined form causes little resistance to the flow, leading to reduced skin friction. Spherical nanoparticles often maintain laminar flow, characterised by smooth and predictable fluid paths, which helps minimise frictional losses. The cylindrical nanoparticles and high skin friction are due to the fact that cylindrical nanoparticles have a

more elongated and projecting form than spherical nanoparticles, resulting in higher surface roughness and disturbance of fluid flow. Cylindrical nanoparticles with edges and corners generate regions of elevated fluid shear and turbulence, leading to higher skin friction. Fluid flow around cylindrical nanoparticles is more likely to shift from laminar to turbulent, leading to chaotic and uneven flow patterns that cause increased frictional losses. The nanoparticles' orientation in relation to the flow direction can impact skin friction. When cylindrical nanoparticles are oriented parallel to the flow, they have a greater cross-sectional area than spherical nanoparticles, resulting in more frictional drag.

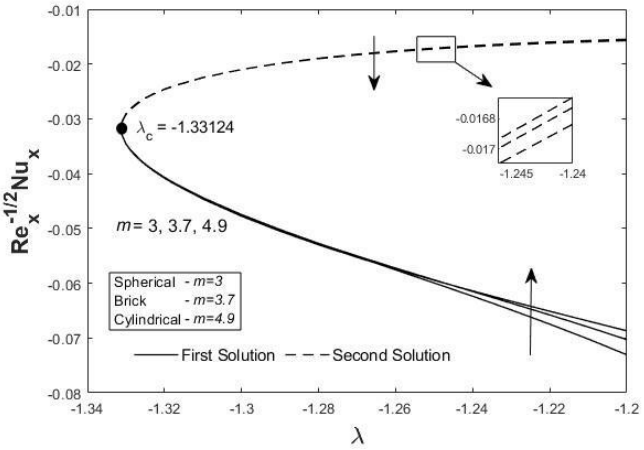


Fig. 3. Nusselt number variation with different types of nanoparticle shapes for the shrinking surface.

Spherical nanoparticles have the lowest Nusselt number compared to cylindrical nanoparticles, with brick forms having values in between, as seen in Figure 3. Understanding this phenomenon involves examining the complex fluid dynamics and heat transmission mechanisms related to various nanoparticle shapes. The spherical nanoparticles have a low Nusselt number due to their smooth and symmetrical shape, which enhances consistent fluid flow around them. The smooth flow patterns around spherical nanoparticles cause little turbulence and mixing in the fluid nearby. Consequently, the convective heat transfer coefficient is lower for spherical nanoparticles, resulting in a decreased Nusselt number. Cylinder nanoparticles have a high Nusselt number because they obstruct the flow more than spherical nanoparticles due to their elongated and projecting form. They improve convective heat transfer by making mixing the fluid around the cylinder-shaped nanoparticles easier. This behaviour leads to a higher Nusselt number because of the higher convective heat transfer coefficient. The brick shapes have an intermediate Nusselt number because the nanoparticles in these shapes have a unique mix of flow properties, and their shape is somewhere between spherical and cylindrical. The brick forms can cause some mixing, although they are usually less disruptive to the flow than cylindrical nanoparticles. The brick-shaped nanoparticles show a moderate convective heat transfer coefficient and Nusselt number compared to spherical and cylindrical nanoparticles. Nanoparticle shape variances affect flow and convective heat transfer rates, which in turn impact the Nusselt number. Spherical nanoparticles have a low Nusselt number due to their smooth flow patterns, while cylindrical nanoparticles have higher convective heat transfer rates, leading to more significant Nusselt numbers. Brick-shaped nanoparticles possess intermediate properties that place them in a medium position for heat transfer efficiency. In order to improve the design and choice of nanoparticles in many heat transfer applications, such as thermal management systems, heat exchangers, and nanofluid-based cooling systems, it is crucial to understand these connections.

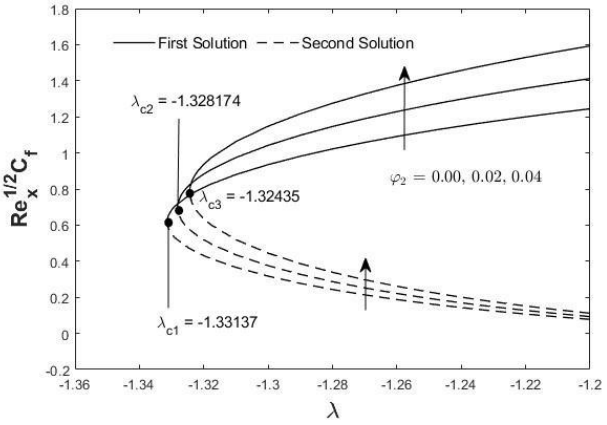


Figure 4. Skin friction variation with different concentrations of MgO for the shrinking surface.

It is essential to determine if a hybrid nanofluid of MgO-Ag-based water can worsen skin friction as the MgO concentration magnifies. This finding could have a significant impact, as shown in Figure 4. It was said that the classical nanofluid Ag-water has less skin friction than when Mg particles are added to the fluid. The possible explanations for this phenomenon happening due to the size and structure of nanoparticles are crucial factors that influence their interaction with fluid flow. The MgO nanoparticles may disturb the flow more strongly than Ag nanoparticles due to their bigger size or unusual shape, resulting in higher skin friction. Moreover, the nanoparticles' surface characteristics, such as roughness and charge, might impact their interaction with the fluid and the boundary layer. MgO nanoparticles with rougher surfaces or differing surface charges compared to Ag nanoparticles might lead to higher skin friction by increasing fluid drag. The extent of aggregation and dispersion in the fluid can influence the nanoparticles' behaviour and their effect on skin friction. Compared to Ag nanoparticles, MgO nanoparticles may have a different tendency to stick together or spread out, which could change the way fluids flow and reduce skin friction. Furthermore, the chemical composition of nanoparticles can affect their compatibility with the base fluid and their capacity to create stable suspensions. Variations in the chemical composition of MgO and Ag nanoparticles can result in variances in fluid characteristics and flow behaviour, which can affect skin friction. The inclusion of nanoparticles can affect the thermal conductivity and viscosity of the nanofluid. Modifications in these characteristics can influence the movement of fluids and the transmission of heat, which might alter skin friction.

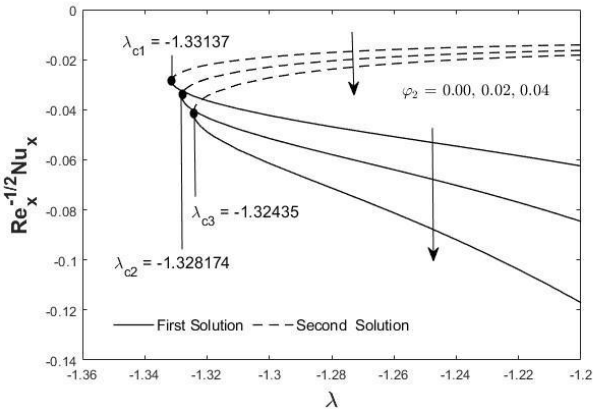


Fig. 5. Nusselt number variation with different concentrations of MgO for the shrinking surface.

The numerical results in Figure 5 show a drop in Nusselt numbers with an increase in MgO concentration, prompting further investigation. Several physical explanations relating to the properties of MgO nanoparticles and their impact on fluid flow and heat transmission help clarify this discovery.

The increased concentration of MgO nanoparticles leads to an increased probability of particle aggregation in the fluid due to hindered flow. Assembled nanoparticles can block flow channels, hindering the passage of fluid molecules and decreasing convective heat transmission. This blockage in flow causes a decrease in the Nusselt number because of a decline in the convective heat transfer coefficient. By adding MgO nanoparticles to the fluid, its viscosity can be changed. Nanoparticles often elevate the viscosity of the base fluid because of their extensive surface area and interactions with fluid molecules. Higher fluid viscosity leads to less fluid movement and slower heat transfer, causing a drop in the Nusselt number. MgO nanoparticles can cause surface roughness in the fluid, especially if they clump together or stick to the walls of the flow channel, leading to boundary layer disturbance. The surface roughness disrupts the flow of the boundary layer near the solid surface, causing an increase in boundary layer thickness and a decrease in convective heat transfer efficiency. The Nusselt number falls with increasing MgO concentration. By adding MgO nanoparticles to the nanofluid, thermal conductivity may change. Nanoparticles usually improve thermal conductivity because of their high thermal conductivity. However, too many particles might reach a saturation point or result in decreasing benefits. When the rise in fluid viscosity is greater than the improvement in thermal conductivity, the total heat transfer efficiency declines, leading to a reduced Nusselt number. When MgO nanoparticles are present in high quantities, they are prone to sedimentation or settling in the fluid, resulting in uneven distribution and decreased suspension stability. Uneven dispersion of nanoparticles impacts the heat transfer process, causing fluctuations in temperature gradients and convective heat transfer rates. As the concentration of MgO increases, the Nusselt number drops. Nusselt numbers go down as the MgO content in the nanofluid goes up. This phenomenon occurs because the flow is slowed, the fluid becomes thicker, the surface is rough, the thermal conductivity changes, and particles settle to the bottom. Comprehending these physical principles is essential for enhancing nanofluid formulations and creating effective heat transfer systems in diverse engineering applications.

Table 5.

Numerical results for skin friction and Nusselt number when opposing and assisting flow as $\lambda = -1.2, Ec = 0.01, \varphi_1 = \varphi_2 = 0.02$.

α	m	M	C_f		Nu_x	
			1st solution	**2nd solution**	**1st solution**	**2nd solution**
-1	3	0	0.918121	0.916186	0.030863	-0.030740
		0.05	1.084938	1.080504	0.045370	-0.045024
		0.1	1.215767	1.208513	0.058470	-0.057806
	3.7	0	1.182487	1.182487	0.030258	-0.030258
		0.05	1.396770	0.237549	0.045452	-0.009757
		0.1	1.565502	0.001314	0.059047	-0.004631
	4.9	0	1.510159	1.510159	0.029820	-0.029820
		0.05	1.782207	1.782207	0.045797	-0.045797
		0.1	1.996871	1.996871	0.060262	-0.060262
-0.5	3	0	0.988941	0.988941	0.035440	-0.035440
		0.05	1.152424	1.152424	0.050871	-0.050871

		0.1	1.283141	1.283141	0.065270	-0.065270
	3.7	0	1.275932	1.275932	0.034676	-0.034676
		0.05	1.486298	1.486298	0.050237	-0.050237
		0.1	1.654819	1.654819	0.064278	-0.064278
	4.9	0	1.631721	1.631721	0.034354	-0.034354
		0.05	1.899882	1.899882	0.050763	-0.050763
		0.1	2.114957	2.114957	0.065685	-0.065685
0	3	0	1.094612	0.274277	0.043786	-0.005303
		0.05	1.255643	0.174176	0.061633	-0.009819
		0.1	1.386857	0.106036	0.078908	-0.015831
	3.7	0	1.405318	0.352130	0.041396	-0.004608
		0.05	1.612057	0.244123	0.057653	-0.010275
		0.1	1.780516	0.136117	0.072523	-0.015942
	4.9	0	1.795317	1.795317	0.041010	-0.041010
		0.05	2.059429	2.059429	0.058047	-0.058047
		0.1	2.274639	2.274639	0.073595	-0.073595
0.5	3	0	1.269744	0.203491	0.063817	-0.006726
		0.05	1.425868	0.169344	0.087465	-0.009747
		0.1	1.555161	0.101051	0.110337	-0.015789
	3.7	0	1.599962	0.343317	0.053098	-0.004460
		0.05	1.800885	0.216976	0.070827	-0.009526
		0.1	1.967627	0.129093	0.087458	-0.015899
	4.9	0	2.031001	0.438606	0.051751	-0.003993
		0.05	2.287749	0.276653	0.069616	-0.009475
		0.1	2.500500	0.164147	0.085990	-0.016169
1	3	0	1.572266	0.042740	0.123352	-0.007000
		0.05	1.706835	0.064110	0.154039	-0.010500
		0.1	1.821488	0.096164	0.182072	-0.015749
	3.7	0	1.913079	0.334874	0.078170	-0.004321
		0.05	2.099297	0.228541	0.099371	-0.010089
		0.1	2.257114	0.122209	0.119604	-0.015857

	4.9	0	2.386571	2.386571	0.070727	-0.070727
		0.05	2.626388	0.267923	0.089592	-0.009404
		0.1	2.829603	0.003092	0.107097	-0.001739

Analysing Table 5 reveals a notable trend in opposing flow scenarios: as the magnetic parameter decreases, there is an apparent reduction in skin friction. This phenomenon can be attributed to the magnetic field's weakening influence on fluid flow, resulting in lower resistance and reduced skin friction. Similarly, the Nusselt number follows a similar pattern, decreasing as the magnetic parameter diminishes. This observation aligns with the reduced heat transfer efficiency in lower magnetic field environments, leading to a lower Nusselt number as the magnetic parameter decreases. Furthermore, an intriguing observation is the comparison of skin friction and Nusselt number among different nanoparticle shapes. Specifically, the skin friction and Nusselt number values for cylinder-shaped nanoparticles are more significant compared to brick and spherical-shaped nanoparticles. This disparity can be attributed to the different flow characteristics and surface interactions associated with each nanoparticle shape. Cylinder-shaped nanoparticles may induce more turbulent flow patterns or experience increased drag, resulting in higher skin friction and enhanced heat transfer, leading to a more significant Nusselt number. Conversely, brick- and spherical-shaped nanoparticles may exhibit smoother flow behaviour and fewer surface interactions, resulting in lower skin friction and reduced heat transfer rates, thus yielding lower Nusselt numbers.

According to the data presented in Table 5, it's clear that there is a noticeable increase in skin friction as the magnetic parameter rises in the case of assisting flow. This phenomenon can be explained by the strengthening influence of the magnetic field on fluid motion, resulting in heightened resistance and, thus, increased skin friction along the surface. Similarly, the Nusselt number follows a parallel trend, demonstrating an enhancement as the magnetic parameter escalates. This trend reflects the improved heat transfer efficiency facilitated by a stronger magnetic field, leading to a higher Nusselt number as the magnetic parameter increases. Furthermore, a notable observation is the comparison of skin friction and Nusselt number across different nanoparticle shapes. Specifically, the skin friction and Nusselt number values for spherical-shaped nanoparticles are more significant compared to brick and cylinder-shaped nanoparticles. This discrepancy can be attributed to the unique flow characteristics and surface interactions associated with each nanoparticle shape. Spherical nanoparticles may induce more turbulent flow patterns, or experience increased drag, resulting in higher skin friction and enhanced heat transfer, leading to a more significant Nusselt number. Conversely, brick and cylinder-shaped nanoparticles may exhibit smoother flow behaviour and fewer surface interactions, resulting in lower skin friction and reduced heat transfer rates, thus yielding lower Nusselt numbers.

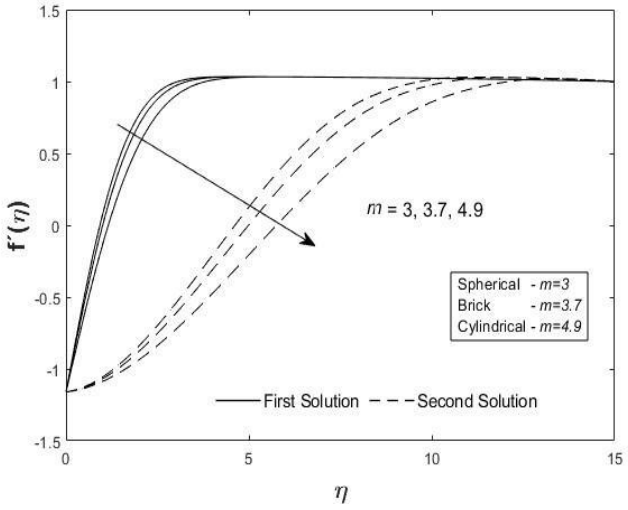


Fig.6. Velocity profile distribution with different types of nanoparticle shapes for the shrinking surface.

The differences in velocity profiles among spherical, brick, and cylindrical nanoparticle shapes in Figure 6 are due to the distinct physical features of each shape and their interaction with fluid flow. Spherical nanoparticles have a smooth and symmetrical geometry that enhances streamlined flow around them. The flat surface of spherical nanoparticles reduces flow disruption, enabling fluid molecules to flow smoothly around them. The velocity profile surrounding spherical nanoparticles is often more consistent and well-defined, with minor flow velocity fluctuations across different fluid parts. Moreover, brick and cylindrical nanoparticles exhibit more intricate and irregular morphologies than spherical nanoparticles. Brick and cylindrical nanoparticles have edges, corners, and protrusions that cause flow disturbances and disrupt the boundary layer near their surfaces. Flow disturbances cause fluctuations in flow velocity and turbulence levels, leading to a less consistent and more disturbed velocity profile than spherical nanoparticles. Further, cylindrical nanoparticles have a greater surface area perpendicular to the flow direction than spherical and brick-shaped nanoparticles. The increased surface area of cylindrical nanoparticles leads to higher drag and frictional resistance as fluid moves around them.

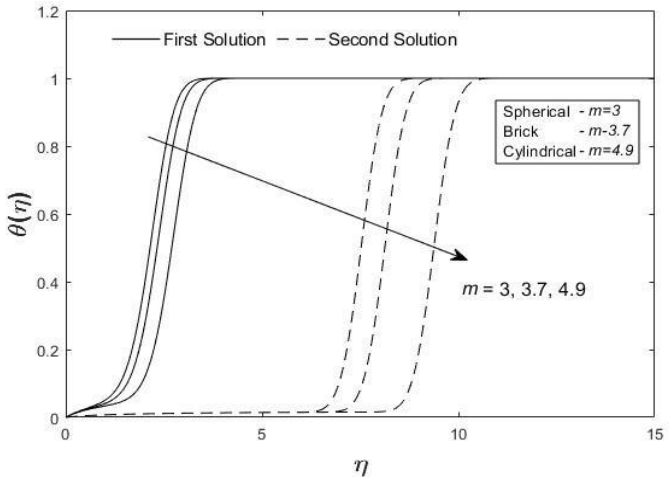


Fig. 7. Temperature profile distribution with different types of nanoparticle shapes for the shrinking surface.

In comparison to spherical and brick nanoparticles, the increased drag and frictional resistance surrounding cylindrical nanoparticles create a more noticeable fall in flow velocity, resulting in a thinner velocity profile. Based on the observations from Fig. 7, the variations in temperature profile

distributions among different nanoparticle shapes can be explained by several factors. These factors include the ratio of surface area to volume, the geometry of the particles, their heat transfer characteristics, the pathways of heat conduction, the contact surface area, and the tendency of particles to pack or agglomerate. Spherical nanoparticles often exhibit the most significant surface area-to-volume ratio compared to other geometries, such as cylinders or bricks. Consequently, spherical nanoparticles possess tremendous surface area per unit volume, enhancing their heat exchange capacity. Therefore, they have the ability to efficiently absorb and disperse heat, resulting in a greater variety of temperature profiles. The morphology of nanoparticles significantly impacts the heat transmission process both inside the nanoparticles themselves and between the nanoparticles and their surrounding environment. Cylindrical nanoparticles have a greater cross-sectional area than spherical ones with the same volume. The increased cross-sectional area enables enhanced heat transmission, promoting more effective heat dissipation along the cylinder's length and reducing temperature profile dispersion. The morphology of nanoparticles influences the routes via which thermal energy is transmitted. Spherical nanoparticles exhibit a higher degree of isotropic heat conduction, resulting in uniform heat distribution in all directions from the surface. Conversely, cylindrical nanoparticles have a preferential heat conduction direction parallel to their length. This phenomenon of directed heat conduction can enhance the efficiency of heat dissipation, leading to a reduction in the overall temperature distribution. The interfacial area between nanoparticles and the surrounding medium is also of paramount importance. For a given volume, spherical nanoparticles often have a lesser contact surface area compared to alternative geometries such as cylinders or bricks. The decreased contact area might lead to less effective heat transfer with the surrounding medium, resulting in a more extensive range of temperature profiles. The nanoparticle form also influences the packing arrangement and susceptibility to aggregation. Spherical nanoparticles have a greater propensity for loose packing and accumulation than other forms. This phenomenon can impact the overall efficiency of heat transport within the medium and, hence, change the distribution of temperature profiles.

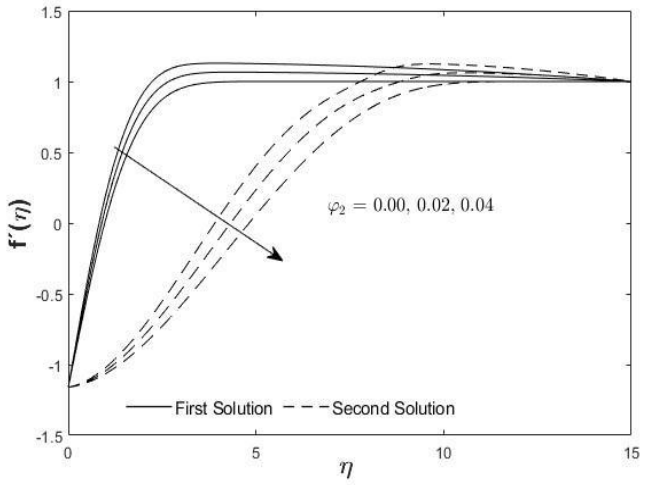


Fig. 8. Velocity profile distribution with different concentrations of MgO for the shrinking surface.

The reduction in velocity profile distribution as the concentration of MgO in the fluid increases is mainly due to the rise in fluid viscosity, disturbance of flow caused by nanoparticles, accumulation of particles, alterations in boundary layer thickness, and potential thermal effects, as shown in Figure 8. The presence of these physical phenomena collectively alters the flow properties and leads to a reduction in the distribution of the velocity profile compared to the nanofluid without MgO. The rise in viscosity is a result of the interaction between the nanoparticles and the molecules of the fluid, which obstructs the fluid's flow. As the concentration of MgO increases, the viscosity of the nanofluid proportionally rises. A rise in viscosity causes more resistance to flow, leading to a decline in the

distribution of velocity profiles. Higher concentrations of MgO nanoparticles lead to a greater probability of particle aggregation inside the nanofluid. Agglomerated particles can cause the formation of small areas with increased thickness and disturb the patterns of movement, resulting in a decrease in the distribution of velocity profiles. Nanoparticles can influence the boundary layer in the vicinity of the flow channel walls. With a rise in the concentration of MgO nanoparticles, the thickness of the boundary layer may also grow as a result of heightened viscosity and flow disruptions generated by the nanoparticles. The presence of a thicker boundary layer reduces the rate of change of velocity near the wall, which in turn causes a drop in the distribution of the velocity profile. The inclusion of MgO nanoparticles in the nanofluid can alter the thermal conductivity and heat transfer capabilities, which in turn can affect the distribution of the velocity profile. Differences in temperature gradients throughout the flow channel can affect the thickness of the fluid and how it flows, resulting in changes to the speed patterns.

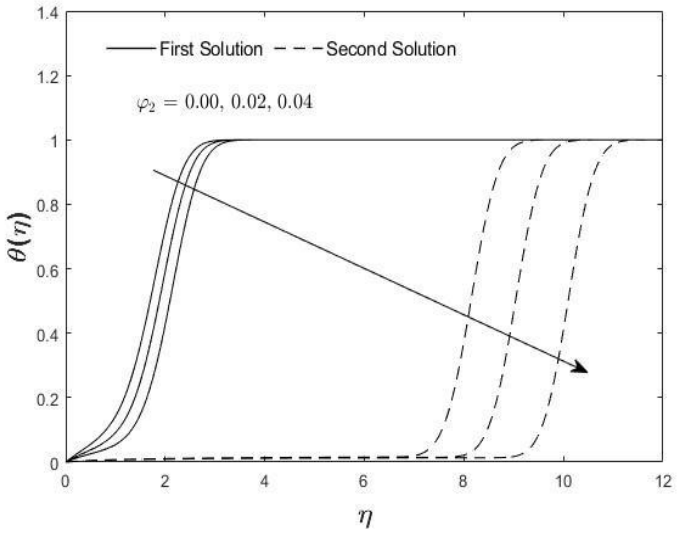


Fig. 9. Temperature profile distribution with different concentrations of MgO for the shrinking surface.

The reduction in temperature profile distribution shown in Figure 9 with increasing concentrations of MgO in the nanofluid can be attributed to several physical phenomena that occur when nanoparticles are added to the fluid. MgO nanoparticles' thermal conductivity is greater than that of the base fluids. When these nanoparticles are evenly distributed in the fluid, they enhance the total thermal conductivity of the nanofluid. With a rise in the concentration of MgO, the number of nanoparticles accessible for enhancing heat transmission also increases. As a consequence, there is enhanced heat conduction and dissipation in the nanofluid, resulting in a reduction in the distribution of temperature profiles. The inclusion of MgO nanoparticles enhances the overall surface area present in the nanofluid. The expanded surface area enables enhanced heat transmission between the fluid and the surrounding environment, resulting in improved efficiency. With a rise in the concentration of MgO, the number of nanoparticles accessible for interaction with the fluid also increases. This phenomenon leads to improved heat transmission and a reduction in the dispersion of temperature profiles. MgO nanoparticles can affect the thickness of the thermal boundary layer near the flow surface. With an increase in the concentration of MgO, the thickness of the boundary layer may decrease as a result of the improved heat transfer capabilities of the nanofluid. A reduced boundary layer thickness facilitates enhanced heat transfer between the fluid and the channel walls, reducing the distribution of temperature profiles. MgO nanoparticles serve as conduits for efficient heat transmission inside the nanofluid. With a rise in the concentration of MgO, the number of channels for conducting heat also increases. This occurrence decreases the total thermal resistance in the nanofluid, enhancing the efficiency of heat conduction and dissipation and reducing the distribution of temperature profiles.

4. Response Surface Methodology (RSM)

The RSM offers an organized and effective strategy to analyse intricate systems that involve several variables. By adhering to these procedures, researchers can acquire a profound understanding of the fundamental connections among variables, optimize process parameters, and enhance the efficiency of systems or processes:

i. Conducting data analysis and data value investigation.
ii. Introducing Mathematical Models for Response Surfaces
iii. Determining the most favourable combination of parameters
iv. Examining the direct and interactive impacts

Based on the numerical analysis, the concentration of MgO and Ag and the shape of nanoparticles influence the skin friction and local Nusselt number (responses). However, statistical data analysis makes it possible to predict the most significant factor contributing to the enhancement of the responses. In this section, the focus is on implementing RSM for a particular spherical nanoparticle shape. Since Wahid et al. [36] have shown that the basic mathematical model is only stable for the first solution, the RSM only focuses on the first solution and ignores the second solution. This study utilizes a face-centred Central Composite Design (CCD) to investigate the relationship between factors and response variables. The design contains three primary components, each with distinct levels, as outlined in Table 6. Table 7 illustrates the RSM with 20 runs for opposing flow, while Table 8 shows the RSM with 20 runs for assisting flow. Based on the data described in Table 6, the correlation is between factors $(\varphi_1, \varphi_2, M)$ and responses (C_f, Nu_x).

Table 6
Levels of parameters for the skin friction and local Nusselt number for opposing and assisting flow.

Parameters	Symbols	Levels		
		Low (-1)	Medium (0)	High (1)
φ_1	A	0.02	0.03	0.04
φ_2	B	0.02	0.03	0.04
M	C	0.0	0.05	0.1

Table 7
RSM with a central composite design for the factors and responses for opposing flow.

Runs	Real values			m=3			Response	
	φ_1	φ_2	M	A	B	C	C_f	Nu_x
1	0.03	0.03	0.1	0	0	1	1.4700518	0.0892496
2	0.04	0.04	0.1	1	1	1	1.5586916	0.101122
3	0.03	0.03	0.05	0	0	0	1.3370131	0.0702876
4	0.03	0.03	0.05	0	0	0	1.3370131	0.0702876
5	0.03	0.02	0.05	0	-1	0	1.2780683	0.0633419
6	0.02	0.04	0	-1	1	-1	1.2048711	0.0544393
7	0.02	0.02	0	-1	-1	-1	1.0919799	0.0435496

8	0.03	0.03	0	0	0	-1	1.1752397	0.0507467
9	0.04	0.02	0	1	-1	-1	1.1450477	0.0472582
10	0.02	0.04	0.1	-1	1	1	1.5056936	0.0958614
11	0.02	0.03	0.05	-1	0	0	1.3112723	0.068078
12	0.04	0.03	0.05	1	0	0	1.3634076	0.0725463
13	0.03	0.03	0.05	0	0	0	1.3370131	0.0702876
14	0.02	0.02	0.1	-1	-1	1	1.3842705	0.0785159
15	0.03	0.03	0.05	0	0	0	1.3370131	0.0702876
16	0.04	0.04	0	1	1	-1	1.2605401	0.0588675
17	0.03	0.03	0.05	0	0	0	1.3370131	0.0702876
18	0.03	0.04	0.05	0	1	0	1.3963831	0.0778707
19	0.03	0.03	0.05	0	0	0	1.3370131	0.0702876
20	0.04	0.02	0.1	1	-1	1	1.4341087	0.083005

Table 8

RSM with a central composite design for the factors and responses for assisting flow.

Runs	**Real data**			**Coded Data**			**Response**	
	φ_1	φ_2	M	**A**	**B**	**C**	C_f	Nu_x
1	0.02	0.02	0	-1	-1	-1	1.097271	0.044026
2	0.04	0.02	0	1	-1	-1	1.150678	0.047799
3	0.02	0.04	0	-1	1	-1	1.211429	0.055184
4	0.04	0.04	0	1	1	-1	1.267498	0.059704
5	0.02	0.02	0.1	-1	-1	1	1.389468	0.079306
6	0.04	0.02	0.1	1	-1	1	1.439635	0.083882
7	0.02	0.04	0.1	-1	1	1	1.512118	0.09706
8	0.04	0.04	0.1	1	1	1	1.565497	0.102431
9	0.02	0.03	0.05	-1	0	0	1.317057	0.068862
10	0.04	0.03	0.05	1	0	0	1.369555	0.073421
11	0.03	0.02	0.05	0	-1	0	1.283421	0.064005
12	0.03	0.04	0.05	0	1	0	1.403005	0.078893
13	0.03	0.03	0	0	0	-1	1.181322	0.051382
14	0.03	0.03	0.1	0	0	1	1.476017	0.090279

15	0.03	0.03	0.05	0	0	0	1.342977	0.071117
16	0.03	0.03	0.05	0	0	0	1.342977	0.071117
17	0.03	0.03	0.05	0	0	0	1.342977	0.071117
18	0.03	0.03	0.05	0	0	0	1.342977	0.071117
19	0.03	0.03	0.05	0	0	0	1.342977	0.071117
20	0.03	0.03	0.05	0	0	0	1.342977	0.071117

The quadratic model used includes three linear terms, three interaction terms, two squared terms, and an intercept term, represented as follows:

$$Regression = a_0 + a_1\,A + a_2\,B + a_3\,C + a_{11}\,A^2 + a_{22}\,B^2 + a_{33}\,C^2 + a_{12}\,A*B + a_{13}\,A*C + a_{23}\,B*C \quad (12)$$

The data analysis was further conducted using Analysis of Variance (ANOVA) through the fit general linear model in statistical analysis Minitab software. The corresponding results are presented in Table 9. Based on Table 9, the P-value for a component B^2 (for C_f) and A^2 (for Nu_x) is more than 0.05 (95% confidence interval); hence, the components must be eliminated. Therefore, the new equations that will be optimized C_f and Nu_x are,

$$C_f = 1.33704 + 0.059270\,A + 0.026371B + 0.147514\,C + 0.000389\,B^2 - 0.014305\,C^2 + 0.000720\,A\,B - 0.000738\,B\,C + 0.002203\,A\,C \quad (13)$$

$$Nu_x = 0.070292 + 0.002235\,A + 0.007249\,B + 0.019289\,C + 0.000321\,A^2 - 0.000287\,C^2 + 0.000186\,A\,B + 0.000202\,B\,C + 0.001620\,A\,C \quad (14)$$

Referring to equation (13), it is evident that skin friction augments as φ_2 increases, which is similar to findings with the numerical solution depicted in Fig. 2. It is a similar occurrence for the Nusselt number to amplify as φ_2 increases, as shown in equation (14). The result for the assisting flow is different from that of the opposing flow. It is evident from Table 10 that the P-value for a component B^2 (for C_f) and A^2 (for Nu_x) is more than 0.05; hence, the components must be eliminated. Therefore, the new equations that will be optimized C_f and Nu_x are

$$C_f = 1.34301 + 0.026552\,A + 0.059907\,B + 0.147454\,C + 0.000400\,A^2 - 0.014237\,C^2 + 0.000734\,A\,B - 0.000741\,A\,C + 0.002192\,B\,C \quad (15)$$

$$Nu_x = 0.071121 + 0.002280\,A + 0.007426\,B + 0.019486\,C + 0.000335\,B^2 - 0.000284\,C^2 + 0.000193\,A\,B + 0.000207\,A\,C + 0.001655\,B\,C \quad (16)$$

It is also eye-catching that from equations (15) and (16), the skin friction and the Nusselt number will amplify when the magnetic parameter is augmented, as illustrated in Table 5.

Table 9
ANOVA for skin friction and Nusselt number when opposing flow.

Source	DF	Adj SS	Adj MS	F-Value	P-Value

C_f					
Model	9	0.260725	0.028969	877009.37	0.000
Linear	3	0.259687	0.086562	2620553.96	0.000
A	1	0.006954	0.006954	210528.63	0.000
B	1	0.035130	0.035130	1063506.23	0.000
C	1	0.217603	0.217603	6587627.03	0.000
Square	3	0.000991	0.000330	9996.62	0.000
A*A	1	0.000000	0.000000	8.22	0.017
B*B	1	0.000000	0.000000	3.33	0.098
C*C	1	0.000569	0.000569	17215.24	0.000
2-Way Interaction	3	0.000047	0.000016	477.52	0.000
A*B	1	0.000004	0.000004	125.59	0.000
A*C	1	0.000004	0.000004	131.76	0.000
B*C	1	0.000039	0.000039	1175.19	0.000
Error	10	0.000000	0.000000		
Lack-of-Fit	5	0.000000	0.000000	*	*
Pure Error	5	0.000000	0.000000		
Total	19	0.260725			
Nu_x					
Model	9	0.004318	0.000480	1044833.59	0.000
Linear	3	0.004296	0.001432	3118542.38	0.000
A	1	0.000050	0.000050	108824.54	0.000
B	1	0.000525	0.000525	1144321.18	0.000
C	1	0.003721	0.003721	8102481.43	0.000
Square	3	0.000000	0.000000	272.52	0.000
A*A	1	0.000000	0.000000	2.26	0.164
B*B	1	0.000000	0.000000	589.02	0.000
C*C	1	0.000000	0.000000	519.54	0.000
2-Way Interaction	3	0.000022	0.000007	15685.85	0.000
A*B	1	0.000000	0.000000	605.15	0.000
A*C	1	0.000000	0.000000	708.16	0.000
B*C	1	0.000021	0.000021	45744.26	0.000
Error	10	0.000000	0.000000		
Lack-of-Fit	5	0.000000	0.000000	*	*
Pure Error	5	0.000000	0.000000		
Total	19	0.004318			

Table 10
ANOVA for skin friction and Nusselt number when assisting flow.

Source	DF	Adj SS	Adj MS	F-Value	P-Value
C_f					
Model	9	0.261393	0.029044	880987.02	0.000
Linear	3	0.260365	0.086788	2632573.85	0.000
A	1	0.007050	0.007050	213850.27	0.000
B	1	0.035889	0.035889	1088626.46	0.000
C	1	0.217426	0.217426	6595244.81	0.000
Square	3	0.000980	0.000327	9910.67	0.000

A*A	1	0.000000	0.000000	8.35	0.016
B*B	1	0.000000	0.000000	4.14	0.069
C*C	1	0.000564	0.000564	17105.98	0.000
2-Way Interaction	3	0.000047	0.000016	476.54	0.000
A*B	1	0.000004	0.000004	130.80	0.000
A*C	1	0.000004	0.000004	133.31	0.000
B*C	1	0.000038	0.000038	1165.50	0.000
Error	10	0.000000	0.000000		
Lack-of-Fit	5	0.000000	0.000000	*	*
Pure Error	5	0.000000	0.000000		
Total	19	0.261393			
Nu_x					
Model	9	0.004424	0.000492	1028116.27	0.000
Linear	3	0.004401	0.001467	3068349.38	0.000
A	1	0.000052	0.000052	108733.95	0.000
B	1	0.000551	0.000551	1153406.70	0.000
C	1	0.003797	0.003797	7942907.48	0.000
Square	3	0.000000	0.000000	274.80	0.000
A*A	1	0.000000	0.000000	2.24	0.166
B*B	1	0.000000	0.000000	616.52	0.000
C*C	1	0.000000	0.000000	487.86	0.000
2-Way Interaction	3	0.000023	0.000008	15724.63	0.000
A*B	1	0.000000	0.000000	622.36	0.000
A*C	1	0.000000	0.000000	714.66	0.000
B*C	1	0.000022	0.000022	45836.86	0.000
Error	10	0.000000	0.000000		
Lack-of-Fit	5	0.000000	0.000000	*	*
Pure Error	5	0.000000	0.000000		
Total	19	0.004424			

It is worth seeing the residual plots before further analysing the performance of skin friction and Nusselt number to determine whether the parameters are suitable for this problem. Fig. 10 depicts the residual plots of the data for skin friction and Nusselt number, respectively. It is clearly seen that for the normal plot, all the data are near the linear line. Moreover, the fitted plots show that the data are scattered, and the bell-shaped histogram indicates that the data is normal distribution. Hence, the data can be further analyzed for performance.

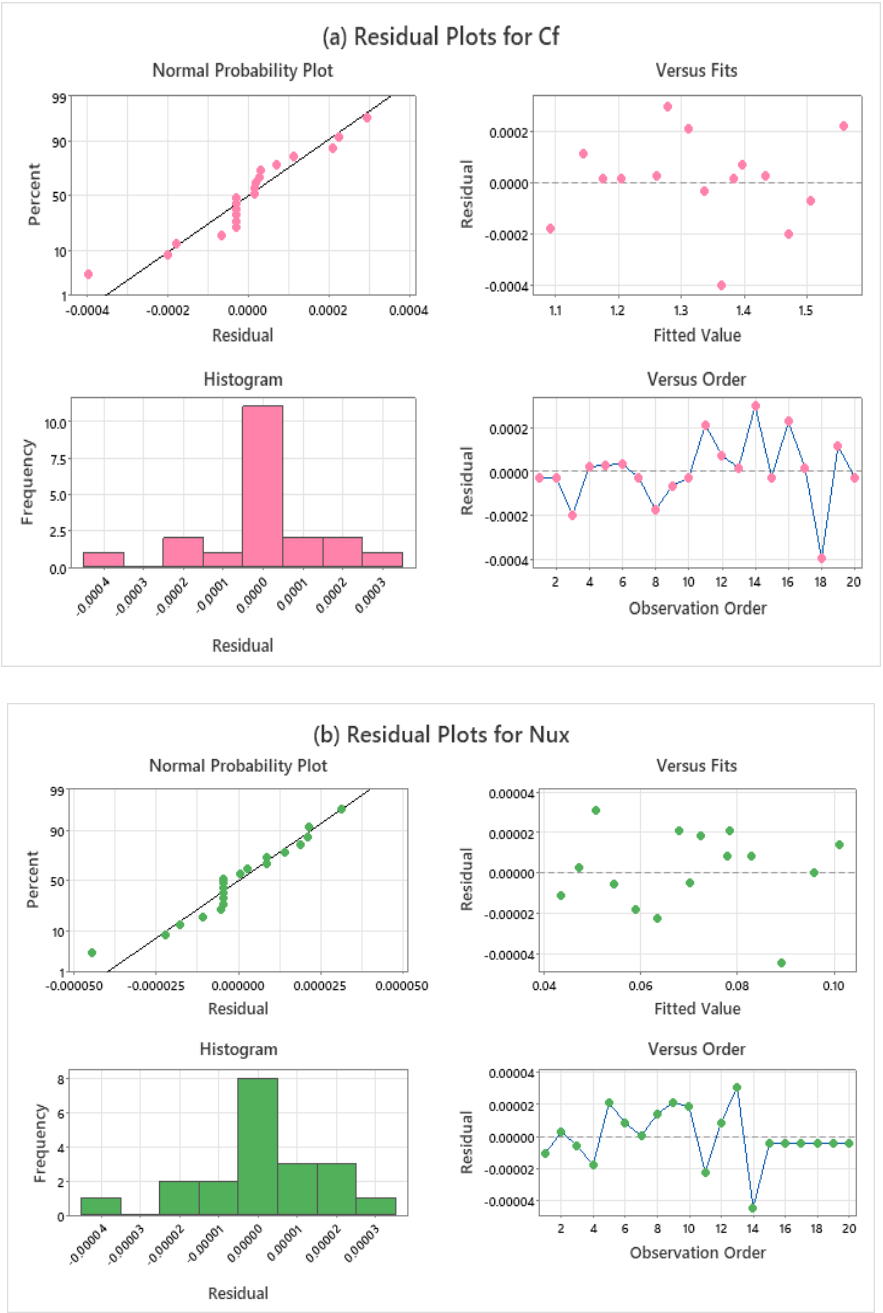


Fig. 10. The residual plots for (a) skin friction and (b) Nusselt number data.

In order to further analyse the performance of skin friction and Nusselt number, Fig. 11 illustrates the contour plots for skin friction and Nusselt number when opposing flow happens. It is clearly seen that the augmented combination of components A and B (φ_1 and φ_2) does not have significant impacts on skin friction and Nusselt number. However, the combination of components B and C (φ_2 and M) produced a tremendous effect on skin friction and Nusselt number.

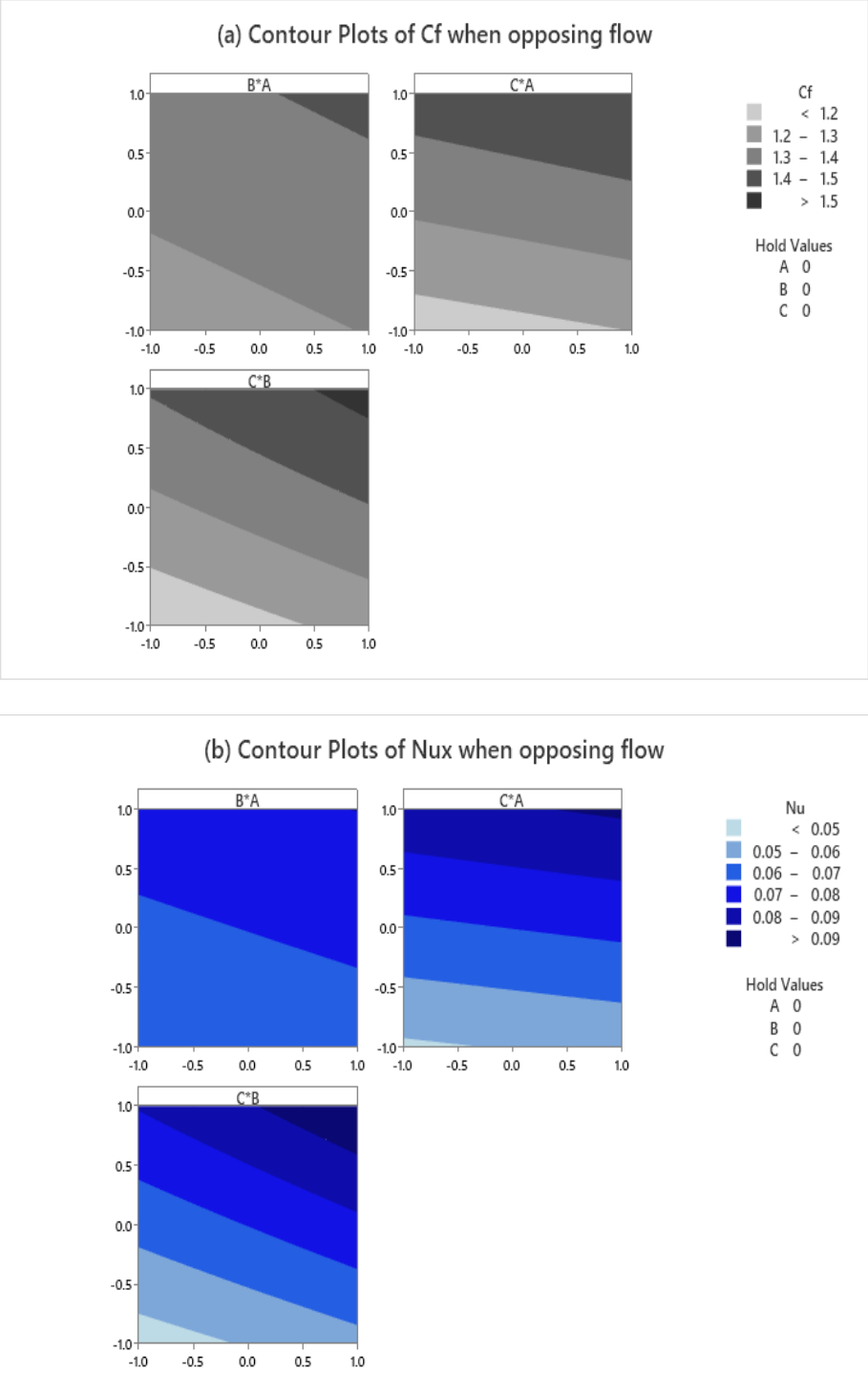


Fig.11. Contour plots of (a) skin friction and (b) Nusselt number when opposing flow.

To determine the optimal combination of two components that yields the highest skin friction and Nusselt number, Fig. 12 presents surface plots specifically for opposing flow scenarios. The visual representation clearly illustrates that the combination of components B and C results in the maximum values for skin friction and Nusselt number. This observation is crucial for understanding the synergistic effects of different components on fluid dynamics and heat transfer. The combination of components B and C likely leads to enhanced turbulence or improved heat transfer properties, resulting in higher skin friction and Nusselt numbers compared to other combinations.

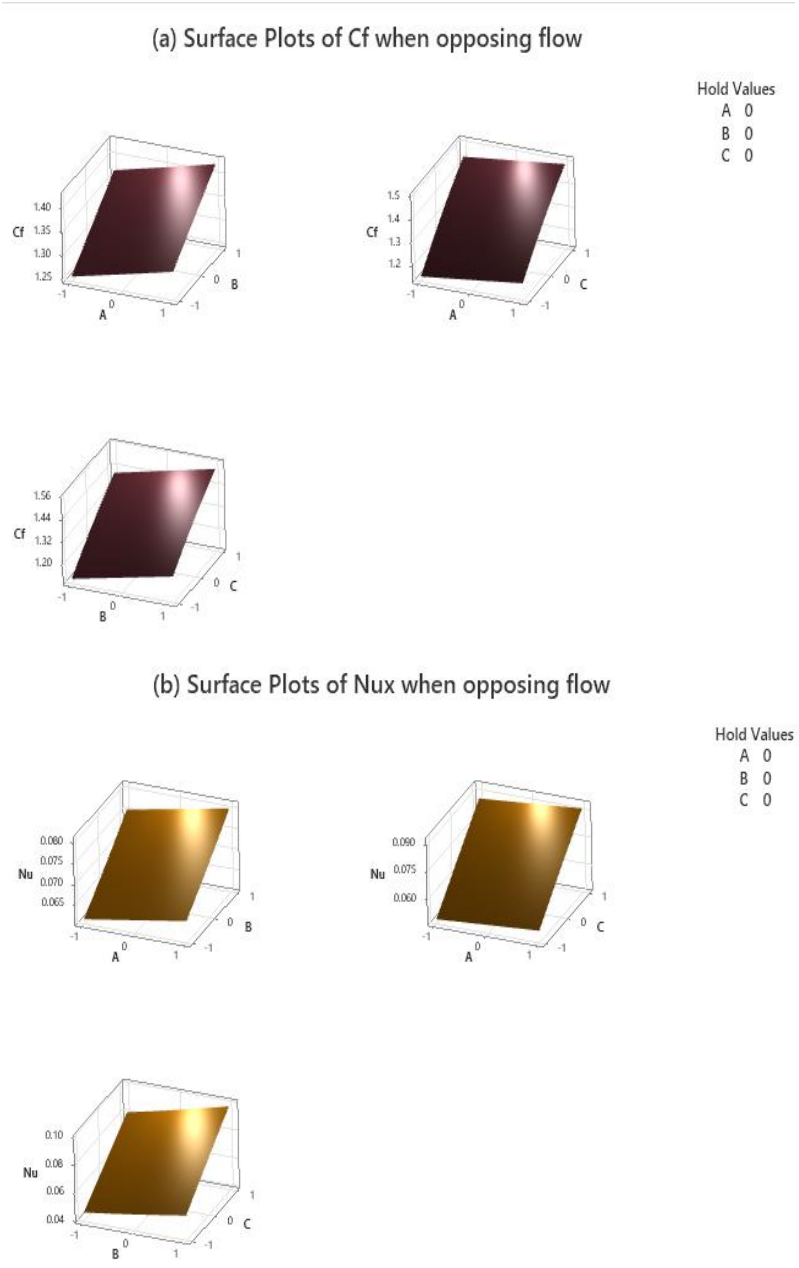


Fig. 12. Surface plots of (a) skin friction and (b) Nusselt number when opposing flow.

When considering assisting flow scenarios, an examination of Figs. 13 and 14 reveals consistent findings akin to those observed in opposing flow conditions. Specifically, it becomes evident that the combination of components B and C consistently leads to the highest values for both skin friction and Nusselt number. This discovery is noteworthy as it underscores the synergistic advantages of utilising components B and C in augmenting fluid dynamics and heat transfer during assisting flow conditions. The notable increase in skin friction and Nusselt number associated with this particular combination suggests improvements in flow characteristics or heightened heat transfer properties when compared to alternative combinations.

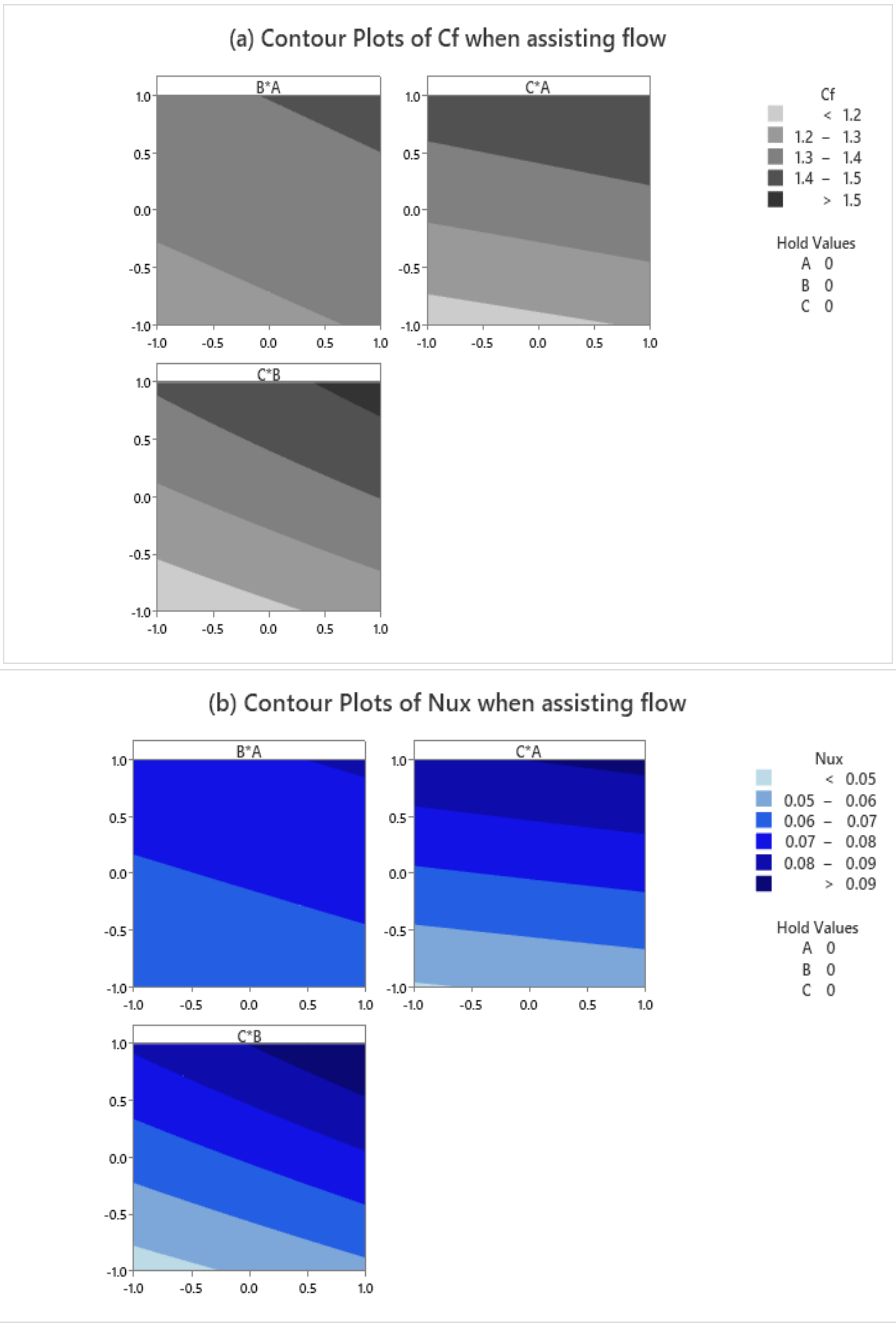


Fig. 13. Contour plots of (a) skin friction and (b) Nusselt number when assisting flow.

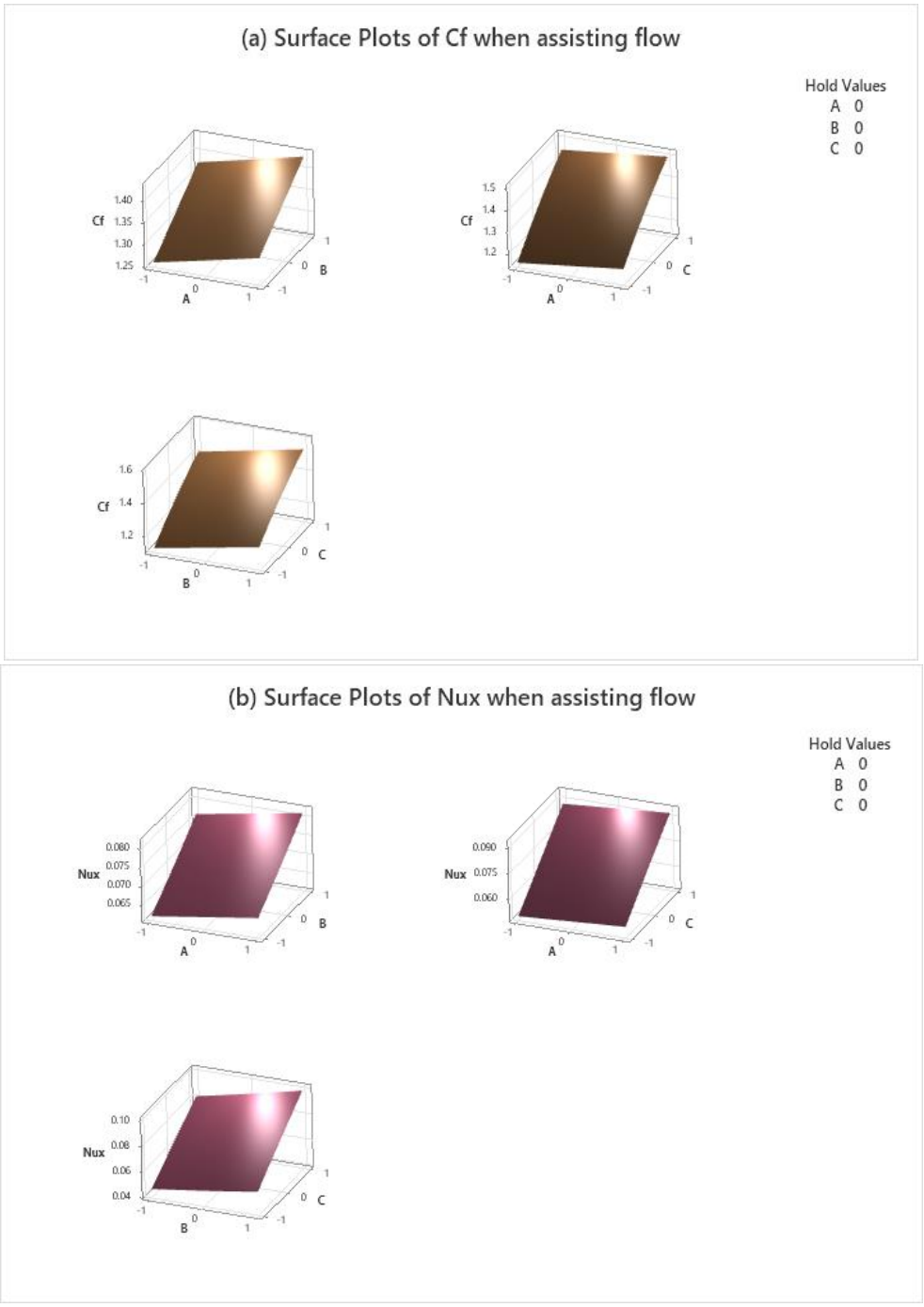


Fig. 14. Surface plots of (a) skin friction and (b) Nusselt number when assisting flow.

Hence, it is also crucial to investigate the optimised combination of three components to produce the desired skin friction and Nusselt number. Based on Table 11, with a desirability of 99.95%, the skin friction for both opposing and assisting flow is optimised at 1.55847 and 1.56527 when the concentrations of Ag, MgO, and magnetic parameters are at their highest levels. The Nusselt number exhibits a comparable trend in assisting flow conditions. According to Table 11, with a desirability of 99.98%, the optimal Nusselt number for both opposing and assisting flows is achieved at values of 0.10110 and 0.102419, respectively, when the concentrations of Ag, MgO, and magnetic parameters are at their peak levels.

Table 11
The optimization of responses

Flow	Responses	A	B	C	Response Fit	Composite Desirability
Opposing	C_f	1	1	1	1.55847	0.999519
	Nu_x	1	1	1	0.101108	0.999755
Assisting	C_f	1	1	1	1.56527	0.999517
	Nu_x	1	1	1	0.102419	0.999790

5. Conclusion

In conclusion, this study has investigated the magnetohydrodynamic (MHD) mixed convection flow and heat transfer of a hybrid nanofluid over a shrinking plate, focusing on the impact of nanoparticle shapes. The methodology involved reducing the governing partial differential equations to ordinary differential equations using similarity transformations and subsequently solving the ODEs numerically using the bvp4c built-in solver in MATLAB software. The findings of this study have provided valuable insights into the influence of various factors on flow and heat transfer characteristics. It was observed that cylindrical nanoparticles exhibit higher skin friction and Nusselt numbers compared to brick and spherical nanoparticles. Additionally, an increase in MgO concentration leads to higher skin friction but lower Nusselt numbers, highlighting the complex interplay between nanoparticle properties and heat transfer behaviour. Furthermore, the effect of magnetic parameters on skin friction and Nusselt numbers was analysed. It was found that the magnetic parameter decreases with skin friction and Nusselt numbers for opposing flow, while an increase in magnetic parameters during assisting flow results in higher skin friction and Nusselt numbers. The study also revealed that spherical-shaped nanoparticles have the highest velocity and temperature profiles compared to brick-shaped and cylindrical-shaped nanoparticles. An increase in MgO concentration was found to reduce velocity and temperature profiles, indicating the importance of nanoparticle concentration in heat transfer enhancement. Finally, based on Response Surface Methodology (RSM), the optimized combination of Ag and MgO concentrations along with magnetic parameters was determined to achieve the highest skin friction and Nusselt numbers. The desirability of 99.95% and 99.98% was achieved for skin friction and Nusselt numbers, respectively, demonstrating the effectiveness of the proposed approach in optimizing flow and heat transfer characteristics under different flow conditions. Overall, this study contributes to the understanding of MHD mixed convection flow and heat transfer in hybrid nanofluids, providing valuable insights for the design and optimization of heat transfer systems involving nanoparticle suspensions.

Author Contributions

For research articles with several authors, a short paragraph specifying their individual contributions must be provided. The following statements should be used “Conceptualization, Nor Ain Azeany Mohd Nasir and Norihan Md Arifin; methodology, Nor Ain Azeany Mohd Nasir and Norihan Md Arifin; software, Nor Ain Azeany Mohd Nasir and Nur Fatin Irwani Muhammad Fadzil.; validation, Nor Ain Azeany Mohd Nasir, Norihan Md Arifin and Nur Syahirah Wahid.; formal analysis, Nor Ain Azeany Mohd Nasir and; investigation, Nor Ain Azeany Mohd Nasir and .; resources, Nor Ain Azeany Mohd Nasir and Nur Fatin Irwani Muhammad Fadzil; data curation, Nor Ain Azeany Mohd Nasir and Rusya Iryanti Yahaya; writing—original draft preparation, Nor Ain Azeany Mohd Nasir; writing—review and editing, Nor Ain Azeany Mohd Nasir, Norihan Md Arifin and Nur Syahirah Wahid;

visualization, Nor Ain Azeany Mohd Nasir, Rusya Iryanti Yahaya and Mohd Syazwan Mohamad Anuar; supervision, Norihan Md Arifin; project administration, Norihan Md Arifin; funding acquisition, Norihan Md Arifin. All authors have read and agreed to the published version of the manuscript." Authorship must be limited to those who have contributed substantially to the work reported.

Data Availability Statement

In this section, please provide details regarding where data supporting reported results can be found, including links to publicly archived datasets analyzed or generated during the study. You might choose to exclude this statement if the study did not report any data.

Conflicts of Interest

Declare conflicts of interest or state "The authors declare that they have no known competing financial interests or personal relationships that could have appeared to influence the work reported in this paper." Authors must identify and declare any personal circumstances or interest that may be perceived as inappropriately influencing the representation or interpretation of reported research results. Any role of the funders in the design of the study; in the collection, analyses or interpretation of data; in the writing of the manuscript, or in the decision to publish the results must be declared in this section. If there is no role, please state "The funders had no role in the design of the study; in the collection, analyses, or interpretation of data; in the writing of the manuscript, or in the decision to publish the results".

Acknowledgement

The authors would like to thank Universiti Putra Malaysia for supporting this research. The Universiti Putra Malaysia funded this research with an Incentive Research Grant

References

[1] Mahmood, Z., Rafique, K., Khan, U., Adnan, El-Rahman, M.A, & Alharbi, R. (2024). Analysis of mixed convective stagnation point flow of hybrid nanofluid over sheet with variable thermal conductivity and slip conditions: A model-based study, *International Journal of Heat and Fluid Flow*, 106 (2024), 109296. https://doi.org/10.1016/j.ijheatfluidflow.2024.109296

[2] Jamrus, F.N., Waini, I., Khan, U., & Ishak, A. (2024). Effects of magnetohydrodynamics and velocity slip on mixed convective flow of thermally stratified ternary hybrid nanofluid over a stretching/shrinking sheet, *Case Studies in Thermal Engineering*, 55, 104161. *Case Studies in Thermal Engineering*, 55, 104161. https://doi.org/10.1016/j.csite.2024.104161

[3] Ummeda P., & Ontela, S. (2023). Irreversibility analysis of magnetohydrodynamic (MHD) mixed convection flow of viscoelastic hybrid nanofluid flow in a channel, *Chemical Engineering Journal Advances*, 16, 100566. https://doi.org/10.1016/j.ceja.2023.100566

[4] Paul, A., Sarma, N., & Patgiri, B.(2023). Mixed convection of shear-thinning hybrid nanofluid flow across a radiative unsteady cone with suction and slip effect, *Materials Today Communications*, 37, 107522. https://doi.org/10.1016/j.mtcomm.2023.107522

[5] Yadav, S., Yadav, S., & Yadav, P.K. (2024). The mixed convection thermally radiated hybrid nanofluid flow through an inclined permeable shrinking plate with slip condition and inclined magnetic effect, *Chinese Journal of Physics*, Doi: 10.1016/j.cjph.2023.12.039. https://doi.org/10.1016/j.cjph.2023.12.039

[6] Rajarathinam, M., Akermi, M., Khan, M.I., & Nithyadevi, N. (2024). MHD mixed convection heat transfer of copper water nanofluid in an inclined porous cavity having isothermal solid block, *Journal of Magnetism and Magnetic Materials*, 593, 171845. https://doi.org/10.1016/j.jmmm.2024.171845

[7] Abood, F.A., Yaseen, S. J., Mohammed, I. G., Homad, R. Z., & Mohammed, H. I. (2024) Enhancing thermal performance in a magnetized square cavity: Novel insights from mixed convection of Ag-MgO nanofluid around a rotating cylinder, *International Journal of Thermofluids*, 22, 100630. https://doi.org/10.1016/j.ijft.2024.100630

[8] Zhang, R., Zaydan, M., Alshehri, M., Raju, C. S. K., Wakif, A., & Shah, N. A. (2024). Further insights into mixed convective boundary layer flows of internally heated Jeffery nanofluids: Stefan's blowing case study with convective heating and thermal radiation impressions, *Case Studies in Thermal Engineering*, 55, 104121. https://doi.org/10.1016/j.csite.2024.104121

[9] Hameed, R. H., Al-Srayyih, B. M., Al-Amir, Q. R., Hamzah, H. K., Ali, F. H, & Alahmer, A. (2024). Magnetic field effect on mixed convection flow inside an oval-shaped annulus enclosure filled by a non-Newtonian nanofluid, *International Journal of Thermofluids*, 21, 100571. https://doi.org/10.1016/j.ijft.2024.100571

[10] Mustafa, J., Alqaed, S., Husain, S., & Sharifpur, M. (2024). Impact of five obstacles with constant temperatures on the mixed convection flow of water/copper nanofluid in a rectangular cavity with a magnetic field, *Results in Physics*, 57, 107424. https://doi.org/10.1016/j.rinp.2024.107424

[11] Hussain, A., Riaz, S., Hassan, A., Malik, M.Y., Alqahtani, A.S., Karamti, H., Saeed, A.M., & Eldin, S.M. (2023). Magneto-bio-convection enhanced heat transfer in Prandtl hybrid nanofluid with inclined magnetization and microorganism migration, *Journal of Magnetism and Magnetic Materials*, 588 (Part A), 171403. https://doi.org/10.1016/j.jmmm.2023.171403

[12] Dinarvand, S., Berehal, H., Tamim, H., Sowmya, G., Noeiaghdam, S., & Abdollahzadeh, M. (2023) Squeezing flow of aqueous CNTs-Fe3O4 hybrid nanofluid through mass-based approach: Effect of heat source/sink, nanoparticle shape, and an oblique magnetic field, *Results in Engineering*, 17, 100976.. https://doi.org/10.1016/j.rineng.2022.100976

[13] Sundar, L.S., & Ramana, E.V. (2023), Influence of magnetic field location on the heat transfer and friction factor of CoFe2O4-BaTiO3/EG hybrid nanofluids in laminar flow: An experimental study, *Journal of Magnetism and Magnetic Materials*, 579 (2023), 170837. https://doi.org/10.1016/j.jmmm.2023.170837

[14] Giwa, S.O., Sharifpur, M., Meyer, J.P., Taziwa, R.T., & Shah, N.A. (2024) Synergetic effect of magnetic field location, strength and orientation on heat transfer characteristics of brine-based hybrid nanofluid in rectangular confinement, *Journal of Magnetism and Magnetic Materials*, 590, 171642. https://doi.org/10.1016/j.jmmm.2024.171642

[15] Mahabaleshwar, U.S., Sachhin, S.M., Perez, L.M., & Oztop, H.F. (2024) An impact of inclined MHD on biviscosity Bingham hybrid nanofluid flow over porous stretching/shrinking sheet with heat transfer, *Journal of Molecular Liquids*, 398, 124244. https://doi.org/10.1016/j.molliq.2024.124244

[16] Sundar, L.S., Alklaibi, A.M., Sambasivam, S., & Mouli, K.V.V.C. (2024). Experimentally determining the thermophysical properties, heat transfer and friction factor Fe3O4-TiO2 magnetic hybrid nanofluids in a mini-heat sink under magnetic field: Proposing new correlations, *Journal of Magnetism and Magnetic Materials*, 594, 171889. https://doi.org/10.1016/j.jmmm.2024.171889

[17] Rajesh, V., & Oztop, H.F. (2024). Conjugate free convection in a non-uniform heating walled enclosure filled by ternary hybrid nanofluid under magnetic field, *Chinese Journal of Physics*, 89, 210-226. https://doi.org/10.1016/j.cjph.2024.03.021

[18] Khan, M.A., Ul-Haq, S., & Ali, F. (2024). Analysis of Newtonian heating in fractional hybrid nanofluid with the influence of transverse magnetic field, *International Journal of Heat and Fluid Flow*, 106, 109293. https://doi.org/10.1016/j.ijheatfluidflow.2024.109293

[19] Dero, S., Fadhel, M.A., Shah, Z., Lund, L.A., Vrinceanu, N., Dewidar, A.Z., & Elansary, H.O. (2023). Multiple solutions of Hiemenz flow of CNTs hybrid base C2H6O2+H2O nanofluid and heat transfer over stretching/shrinking surface: Stability analysis, *Case Studies in Thermal Engineering*, 49, 103190. https://doi.org/10.1016/j.csite.2023.103190

[20] Yahaya, R.I., Mustafa, M.S., Arifin, N.M., Pop, I., Ali, F.M., & Isa, S.S.P.M.(2023). Hybrid nanofluid flow past a biaxial stretching/shrinking permeable surface with radiation effect: Stability analysis and heat transfer optimization, *Chinese Journal of Physics*, 85, 402-420. https://doi.org/10.1016/j.cjph.2023.06.018

[21] Hafeez, A., Aldosari, F.M., Helmi, M.M., Ghazwani, H.A., Hussien, M., & Hassan, A.M. (2023). Heat transfer performance in a Hybrid nanofluid (Cu-Al2O3 /kerosene oil) flow over a shrinking cylinder, *Case Studies in Thermal Engineering*, 52, 103539. https://doi.org/10.1016/j.csite.2023.103539

[22] Jaafar, A., Jamaludin, A., Nasir, N.A. A. M., Nazar, R. & Pop, I. (2023). MHD opposing flow of Cu-TiO2 hybrid nanofluid under an exponentially stretching/shrinking surface embedded in porous media with heat source and slip impacts, *Results in Engineering*, 17, 101005. https://doi.org/10.1016/j.rineng.2022.101005

[23] Yasir, M., Khan, M., Alqahtani, A. S. & Malik, M. Y. (2023). Mass transpiration effect on rotating flow of radiative hybrid nanofluid due to shrinking surface with irregular heat source/sink, *Case Studies in Thermal Engineering,* 44, 102870. https://doi.org/10.1016/j.csite.2023.102870

[24] Waini, I., Alabdulhady, S., Ishak, A. & Pop, I. (2023). Viscous dissipation effects on hybrid nanofluid flow over a non-linearly shrinking sheet with power-law velocity, *Heliyon*, 9(10), e20910. https://doi.org/10.1016/j.heliyon.2023.e20910

[25] Roy, N.C. & Akter, A. (2023). Dual solutions of mixed convective hybrid nanofluid flow over a shrinking cylinder placed in a porous medium, *Heliyon*, 9(11), e22166. https://doi.org/10.1016/j.heliyon.2023.e22166

[26] Saleem, S., Ahmad, B., Naseem, A., Riaz, M. B. & Abbas, T. (2024). Mono and hybrid nanofluid analysis over shrinking surface with thermal radiation: A numerical approach, *Case Studies in Thermal Engineering*, 54, 104023. https://doi.org/10.1016/j.csite.2024.104023

[27] Shah, Z., Asghar, A., Ying, T. Y., Lund, L. A., Alshehri, A. & Vrinceanu, N. (2024). Numerical investigation of sodium alginate-alumina/copper radiative hybrid nanofluid flow over a power law stretching/shrinking sheet with

suction effect: A study of dual solutions, *Results in Engineering*, 21, 101881. https://doi.org/10.1016/j.rineng.2024.101881

[28] Asifa, A. T., Kumam, P. & Muhammad, S. (2022). New fractional model to analyze impacts of Newtonian heating, shape factor and ramped flow function on MgO-SiO2-Kerosene oil hybrid nanofluid, *Case Studies in Thermal Engineering*, 38, 102361. https://doi.org/10.1016/j.csite.2022.102361

[29] Anwar, T., Asifa, & Kumam, P. (2022). A fractal fractional model for thermal analysis of GO − NaAlg − Gr hybrid nanofluid flow in a channel considering shape effects, *Case Studies in Thermal Engineering*, 31, 101828. https://doi.org/10.1016/j.csite.2022.101828

[30] Rafique, K., Mahmood, Z., Saleem, S., Eldin, S.M., and Khan, U. (2023). Impact of nanoparticle shape on entropy production of nanofluid over permeable MHD stretching sheet at quadratic velocity and viscous dissipation, *Case Studies in Thermal Engineering*, 45, 102992. https://doi.org/10.1016/j.csite.2023.102992

[31] Kezzar, M., Talbi, N., Sari, M. R., Nehal, A., Sharifpur, M., Kumar, R., Gharib, N., Salsoul, W. & Fatiha, H. (2023). Velocity-slip boundary conditions and shape factor effects on MHD hybrid nanofluid flow via converging/diverging channels, *Journal of Magnetism and Magnetic Materials*, 587, 171215. https://doi.org/10.1016/j.jmmm.2023.171215

[32] Rahman, M., Turkyilmazoglu, M. & Matloob, K. (2023). Impact of multiple shapes on Al2O3-Cu/H2O-C_2H6O_2 towards a permeable surface of cylinder, *Journal of Magnetism and Magnetic Materials*, 581, 170965. https://doi.org/10.1016/j.jmmm.2023.170965

[33] Jeevankumar & Sandeep, N. (2024). Computational analysis to examine the role of nanoparticle shape on operative usage of solar energy, *International Journal of Hydrogen Energy*, 56, 937-948. https://doi.org/10.1016/j.ijhydene.2023.11.256

[34] Ragupathi, E., Prakash, D., Muthtamilselvan, M. & Al-Mdallal, Q. M. (2024). A case study on heat transport of electrically conducting water based-CoFe2O4 ferrofluid flow over the disc with various nanoparticle shapes and highly oscillating magnetic field, *Journal of Magnetism and Magnetic Materials*, 589, 171624. https://doi.org/10.1016/j.jmmm.2024.171624

[35] Yahyaee, A. (2024). Influence of nanoparticle shapes in nanofluid film boiling on vertical cylinders: A numerical study, *International Journal of Thermofluids*, 22, 100631. https://doi.org/10.1016/j.ijft.2024.100631

[36] Wahid N. S., Arifin N. M., Pop I., Bachok N. & Hafidzuddin M. E. H. (2022). MHD stagnation-point flow of nanofluid due to a shrinking sheet with melting, viscous dissipation and Joule heating effects, *Alexandria Engineering Journal* 61(12), 12661–12672. https://doi.org/10.1016/j.aej.2022.05.050

[37] Khashi'ie, N. S., Arifin, N. M., Nazar, R., Hafidzuddin, E. H., Wahi, N. & Pop, I. (2019). Mixed Convective Flow and Heat Transfer of a Dual Stratified Micropolar Fluid Induced by a Permeable stretching/Shrinking Sheet, *Entropy*, 21, 1162. https://doi.org/10.3390/e21121162

[38] Sarfraz M., Yasir M., and Khan M. (2023). Multiple solutions for non-linear radiative mixed convective hybrid nanofluid flow over an exponentially shrinking surface,*Scientific Reports* 13, 3443. https://doi.org/10.1038/s41598-023-30548-5

[39] Redouane F., Jamshed W., Devi S. S.U., Prakash M., Nasir N. A. A. M, Hammouch Z., Eid M. R., Nisar K.S., Mohammed A, B., Abdel-Aty A., Yahia I. S. & Eed EM. (2022). Heat flow saturate of Ag/MgO-water hybrid nanofluid in heated trigonal enclosure with rotate cylindrical cavity by using Galerkin finite element, *Scientific Reports* 12, 2302. https://doi.org/10.1038/s41598-022-06385-3

[40] Alabdulhadi S., Bakar S.A., Ishak A., Waini I. & Ahmed SE. Effect of buoyancy force on an unsteady thin film flow of Al2O3/water nanofluid over an inclined stretching sheet, *Mathematics* 11(3) (2023) 739. https://doi.org/10.3390/math11030739

[41] Bachok N., Ishak A. & Pop I. (2010) Melting heat transfer in boundary layer stagnation-point flow towards a stretching/shrinking sheet, *Physics Letters A*, 374(40), 4075–4079. https://doi.org/10.1016/j.physleta.2010.08.032

JMMME
JOURNAL OF MATHEMATICAL MODELS AND METHODS IN ENGINEERING

CONTENTS

00010	**Comparing Stochastic Training Environments for Deep Reinforcement Learning with Deep Q-network: Learning Stability and Transfer to Real Data** Yuriy Yurchenko, Dr. Olexandr Zakovorotnyi (Author)	4–18
00011	**Optimization of Irrigation Systems and Ecological Assessment: A Case Study of Andijan Region, with a Forecast to 2032** Ibrohimjon Abdurahmonov (Author)	19–28
00012	**Evaluation of Cement Production for Continuous and Discrete Flow Systems by Applying a Discrete Event Simulation Approach** Wan Laailatul, Mohd Kamal Nawawi, Nur Anis Hannan Md Shahid (Author)	29–35
00013	**Optimization of Heat Transfer in MHD Mixed Convection Hybrid Nanofluid Flow Over a Shrinking Plate Using Response Surface Methodology** NORIHAN MD ARIFIN, Nor Ain Azeany Mohd Nasir, Nur Fatin Irwani Muhammad Fadzil, Rusya Iryanti Yahya, Nur Syahirah Wahid, Mohd Syazwan Mohamad Anuar (Author)	36–65
00014	**An Automatic Quadrature Scheme for Bounded and Unbounded Weighted Hypersingular Integrals on the Variable Interval** Zainidin Eshkuvatov (Author)	66–80
00015	**A boundary value problem with a conormal derivative and a nonlocal integral condition for a degenerate elliptic equation of the second kind** Akmaljon Abdullaev (Author)	81–97